



Constitutive Modeling of the Facesheet to Core Interface in Honeycomb Sandwich Panels Subject to Mode I Delamination

Daniel Höwer

Institute of Applied Mechanics, RWTH Aachen University, Aachen, Germany

Bradley A. Lerch, Brett A. Bednarczyk, and Evan J. Pineda

Glenn Research Center, Cleveland, Ohio

Stefanie Reese and Jaan-Willem Simon

Institute of Applied Mechanics, RWTH Aachen University, Aachen, Germany

NASA STI Program . . . in Profile

Since its founding, NASA has been dedicated to the advancement of aeronautics and space science. The NASA Scientific and Technical Information (STI) Program plays a key part in helping NASA maintain this important role.

The NASA STI Program operates under the auspices of the Agency Chief Information Officer. It collects, organizes, provides for archiving, and disseminates NASA's STI. The NASA STI Program provides access to the NASA Technical Report Server—Registered (NTRS Reg) and NASA Technical Report Server—Public (NTRS) thus providing one of the largest collections of aeronautical and space science STI in the world. Results are published in both non-NASA channels and by NASA in the NASA STI Report Series, which includes the following report types:

- **TECHNICAL PUBLICATION.** Reports of completed research or a major significant phase of research that present the results of NASA programs and include extensive data or theoretical analysis. Includes compilations of significant scientific and technical data and information deemed to be of continuing reference value. NASA counter-part of peer-reviewed formal professional papers, but has less stringent limitations on manuscript length and extent of graphic presentations.
- **TECHNICAL MEMORANDUM.** Scientific and technical findings that are preliminary or of specialized interest, e.g., “quick-release” reports, working papers, and bibliographies that contain minimal annotation. Does not contain extensive analysis.
- **CONTRACTOR REPORT.** Scientific and technical findings by NASA-sponsored contractors and grantees.
- **CONFERENCE PUBLICATION.** Collected papers from scientific and technical conferences, symposia, seminars, or other meetings sponsored or co-sponsored by NASA.
- **SPECIAL PUBLICATION.** Scientific, technical, or historical information from NASA programs, projects, and missions, often concerned with subjects having substantial public interest.
- **TECHNICAL TRANSLATION.** English-language translations of foreign scientific and technical material pertinent to NASA's mission.

For more information about the NASA STI program, see the following:

- Access the NASA STI program home page at <http://www.sti.nasa.gov>
- E-mail your question to help@sti.nasa.gov
- Fax your question to the NASA STI Information Desk at 757-864-6500
- Telephone the NASA STI Information Desk at 757-864-9658
- Write to:
NASA STI Program
Mail Stop 148
NASA Langley Research Center
Hampton, VA 23681-2199



Constitutive Modeling of the Facesheet to Core Interface in Honeycomb Sandwich Panels Subject to Mode I Delamination

Daniel Höwer

Institute of Applied Mechanics, RWTH Aachen University, Aachen, Germany

Bradley A. Lerch, Brett A. Bednarczyk, and Evan J. Pineda

Glenn Research Center, Cleveland, Ohio

Stefanie Reese and Jaan-Willem Simon

Institute of Applied Mechanics, RWTH Aachen University, Aachen, Germany

National Aeronautics and
Space Administration

Glenn Research Center
Cleveland, Ohio 44135

Acknowledgments

The first author is funded by the Excellence Initiative of the German federal and state governments. E. J. Pineda acknowledges funding through the von Kármán fellowship GS069. Funding by the Ministry of Innovation, Science and Research of the State of North Rhine-Westphalia is acknowledged by J.-W. Simon. The authors thankfully acknowledge the assistance of Anna D. Schiffer and Timo D.E. Sirinyan who helped with the parameter study and data reduction.

Trade names and trademarks are used in this report for identification only. Their usage does not constitute an official endorsement, either expressed or implied, by the National Aeronautics and Space Administration.

Level of Review: This material has been technically reviewed by technical management.

Available from

NASA STI Program
Mail Stop 148
NASA Langley Research Center
Hampton, VA 23681-2199

National Technical Information Service
5285 Port Royal Road
Springfield, VA 22161
703-605-6000

This report is available in electronic form at <http://www.sti.nasa.gov/> and <http://ntrs.nasa.gov/>

Abstract

A new cohesive zone traction-separation law, which includes the effects of fiber bridging, has been developed, implemented with a finite element (FE) model, and applied to simulate the delamination between the facesheet and core of a composite honeycomb sandwich panel. The proposed traction-separation law includes a standard initial cohesive component, which accounts for the initial interfacial stiffness and energy release rate, along with a new component to account for the fiber bridging contribution to the delamination process. Single Cantilever Beam tests on aluminum honeycomb sandwich panels with carbon fiber reinforced polymer facesheets were used to characterize and evaluate the new formulation and its finite element implementation. These tests, designed to evaluate the mode I toughness of the facesheet to core interface, exhibited significant fiber bridging and large crack process zones, giving rise to a concave downward / concave upward pre-peak shape in the load-displacement curve. Unlike standard cohesive formulations, the proposed formulation captures this observed shape, and its results have been shown to be in excellent quantitative agreement with experimental load-displacement results and apparent critical energy release rate results, representative of a payload fairing structure, as well as local strain fields measured with digital image correlation.

1 Introduction

Payload fairings are large shell structures mounted atop launch vehicles that protect the payload from aerodynamic and acoustic loads during launch. They must separate cleanly from the vehicle after launch, without the possibility of re-contact. The baseline design of the payload fairing for NASA's Space Launch Systems (SLS) heavy lift vehicle involves separable petals composed of aluminum honeycomb sandwich panels with carbon fiber reinforced polymer facesheets. Pre-existing flaws from manufacturing defects or damage during handling, assembly, payload encapsulation, vehicle integration and launch can jeopardize the expected life and performance of honeycomb structures like the SLS fairing. While damage detected through non-destructive evaluation prior to launch will be repaired, the presence of undetected damage, as well as damage occurring during launch, cannot be ruled out. Therefore, damage tolerance is a key component of the SLS fairing design.

Low-speed impacts, such as tool drops or unintended contact with ground support equipment, are the most prevalent cause of post-manufacturing damage. For honeycomb sandwich structures, low-speed impacts result in core crushing, delamination/disbonds, and matrix cracking [1, 2]. Subsequent loading can lead to kink band formation (fiber microbuckling), indentation (core crushing growth), and delamination/disbond growth [1–4]. Compression after impact (CAI) tests are a typical method for quantifying the effect of such damage on composite honeycomb sandwich panels. CAI tests produce a reduced design-to strength allowable for the honeycomb panel composite facesheets, providing damage tolerance for strength-driven designs [5, 6]. However, the acreage payload fairing panel design is buckling-dominated, with local stresses at the buckling failure loads being several times lower

than the strength allowable [7–9]. As such, understanding the failure mechanisms associated with damage and buckling is critical for providing damage tolerance to large composite honeycomb sandwich structures like the SLS fairing.

The present work focuses on the delamination/disbond failure mechanism in damaged composite honeycomb panels. Disbond growth may occur in large composite honeycomb sandwich panels prior to, or in conjunction with, panel buckling [10]. To include this mechanism in finite element panel buckling simulations, a characterized cohesive zone model is needed that can accurately model the facesheet to core interfacial behavior. Towards this end, the growth of disbonds between the facesheets and the aluminum honeycomb core is investigated herein via Single Cantilever Beam (SCB) tests and employing a new cohesive zone model that accounts for the extensive bridging observed during the SCB testing.

Numerically, delamination is commonly described by cohesive zone models (CZMs), which relate the traction across the crack to the corresponding separation. There are various formulations for cohesive laws, including bilinear [11, 12], tri-linear [13–18], quadratic [19], square root [20], exponential [21, 22] and general power laws [23, 24]. The traction-separation law is generally implemented in zero thickness element formulations, which lack many conventional continuum element properties such as lateral contraction. The resulting spring-like formulation is well-suited for the high element aspect ratios encountered in thin cohesive layer problems. Consistent engineering solutions are obtained when the length of the process zone is several times the characteristic element length and the crack is thus “smeared” over multiple elements [25].

Alternatively delamination has been modeled in a finite thickness framework, e.g. [26–29]. It has recently been demonstrated that the numerical challenges posed by the involved aspect ratios can be alleviated by employing solid-shell element formulations [30, 31]. However, in the presence of fiber bridging, traction is transferred even at very large separations, which leads to non-zero stress at unreasonably high strains in the continuum damage mechanics framework.

Fiber bridging has been investigated in a CZM framework multiple times with various foci. In [13–15] Li et al. propose a tri-linear model in which the model parameters are related to matrix cracking and fiber bridging and apply the cohesive relationship to a composite with random fiber orientation. A similar approach is followed by Dávila et al. [16] for the modeling of a compact tension specimen where the fibers are aligned in load direction and by for instance Heidari-Rarani et al. or Airolidi and Dávila [17, 32] who use the approach for fibers which are initially perpendicular to the loading direction of the Double Cantilever Beam (DCB) specimen, i.e., in crack growth direction.

Xie et al. [33] propose a constitutive law in which the traction-separation law is bilinear, but the critical energy release rate (CERR), which is proportional to the area under the curve, is dependent on the crack length. This is done in order to address the apparent increase of CERR over the crack length observed in specimens that exhibit fiber bridging. However, this method is not applicable if the crack onset point is not a priori known. Wong et al. [34] compare cohesive laws with exponential and tri-linear softening having relatively long tails. They find exponential softening to give more modeling flexibility.

An alternative way to evaluate the CERR without explicitly monitoring the crack front is offered through extensions of Rice’s J integral [35]. This has for instance been shown for mode I delamination by Sørensen and Jacobsen [20, 36], where a specific shape for the cohesive law up to a free parameter is still assumed. However, as demonstrated by Leone et al. [37], the J integral can also be used to directly determine the cohesive law and CERR directly from experimental data for the DCB (mode I) and End Notched Flexure (mode II) specimen, without applying assumptions on the cohesive law. The method has recently been applied in conjunction with digital image correlation (DIC) measurements by Leone et al. for the design of composite joints [38]. The approach has been further refined to reliably predict the CERR of mixed mode bending specimens by Sarrado et al. [39], again relying on DIC measurements as DIC allows for very accurate monitoring of the normal and tangential openings as well as the leg rotations. Since detailed DIC data were obtained for the present work, transferring the method to SCB specimen could be a logical continuation for future work.

Furthermore, a dependence of the amount of fiber bridging on the strain rate was observed by Cantwell et al. [40] who investigated a sandwich panel subjected to three point bending. Since the CERR was found to be primarily driven by the amount of fiber bridging therein, the mean values of the CERR also varied considerably. Higher strain rates were associated with lower CERR and less fiber bridging and vice versa.

Another challenge is posed by the relatively high load-displacement scatter observed when substantial amounts of fiber bridging are observed [33, 41]. This has been numerically addressed by stochastic cohesive zone modeling where the parameters of the cohesive law are varied. For instance Shanmugam et al. [41] use the latin hypercube method to obtain randomized parameters for the formulation proposed by Feih [23], which is a cohesive zone formulation of the fiber pull-out described by Hsueh [42]. While the cumulative load distribution function of the observed experimental loads could be approximated well, the authors note that the cumulative distribution functions of the (apparent) CERR and, to an even larger extent, the crack length curve, could not be matched very well.

In the previously discussed cases of layered composites, the fiber bridging is mostly stochastic. A notable exception are stitched composites, which are designed to take advantage of fiber bridging. Furthermore, the bridging length is well-defined and known a priori. Tan et al. [43] modeled this material system by spring-like elements with non-linear constitutive behavior that were added at the nodes of the cohesive elements. Several phases of the response, such as interfacial debonding and frictional pull-out, were identified and are reflected in the constitutive law. In the case of stitched composites, load drops are linked to the stitching length, whereas load drops in non-stitched composites are neither consistent from load drop to load drop nor from specimen to specimen. The load drops correspond to bridging fibers that eventually fail [33, 34, 44], an inherently stochastic process.

Canal et al. [45] investigate fiber bridging by means of the embedded cells approach. This has the advantage of just considering one local, small-scale failure mechanism multiple times rather than a number of large-scale mechanisms at once. One of the main findings of the authors is that the apparent fracture toughness of the interface

depends almost linearly on the strength of the traction-separation law employed between bridging bundles but hardly on the chosen toughness.

Mostly, the levers of DCB or SCB specimen are considered perfectly elastic. However, Goutianos and Sørensen [46] point out, that the lever of a DCB setup could also exhibit large scale plasticity, and show that the effect can be resolved through a J-integral-based approach with acceptable error.

All of these approaches have in common that the cohesive formulation assumes a maximum stress value, i.e. the strength, at very small separations compared to the failure separation. This property, in conjunction with the fact that the area under the curve is given by the CERR, typically leads to a fairly short process zone in most applications [25]. By shifting the strength of a two-parameter model to very low values, or by choosing a low CERR of the high strength part of a trilinear law, it is possible to extend the process zone length [13,14]. However, even in this case, the tractions at larger separations tend to be low. It has been observed many times that the CERR associated with bridged delamination can be considerably higher than the fracture toughness associated with unbridged delamination [17, 47, 48]. This raises the question, if a cohesive law, which assumes the highest traction at a relatively high separation, may be suitable for delamination in the presence of severe fiber bridging.

Towards this end, a cohesive law, which separately treats the initial low-separation cracking/splitting and the high separation bridging and snapping, is proposed. The best agreement with test data was achieved when the high separation (bridging) part strength was considerably higher than the low-separation initial component.

2 Cohesive law accounting for fiber bridging

2.1 Motivation, failure mechanism, and qualitative cohesive law

In the current work, it is assumed that the total normal cohesive traction T_c can be additively split into two regimes that are each represented by a separate cohesive law. Thus, the total traction reads

$$T_c(\delta_n) = T_m(\delta_n) + T_b(\delta_n) \quad (1)$$

The traction T_m indicates the cohesive component, which is related to the initial stiffness, strength, and CERR of the interface. The index m is chosen because the interface properties are mostly related to the matrix/adhesive strength and CERR. δ_n denotes the normal separation. This regime can be modeled with established formulations, e.g. [11]. In this work, a constant penalty stiffness prior to damage onset and exponential softening subsequent to damage onset is chosen as proposed in e.g. [21, 22], see Figure 1. T_m represents the mechanism shown in Figure 2 Stage I. The bridging part of the cohesive law T_b accounts for the stages II-IV in Figure 2. It reflects the fact that bridging fiber bundles/lamina only transfer a significant traction once they are sufficiently aligned with the loading direction. The process zone of length l_{PZ} , which is in this work defined as the zone where damage has occurred, but total decohesion has not yet occurred, is shown in Figure 2. The range

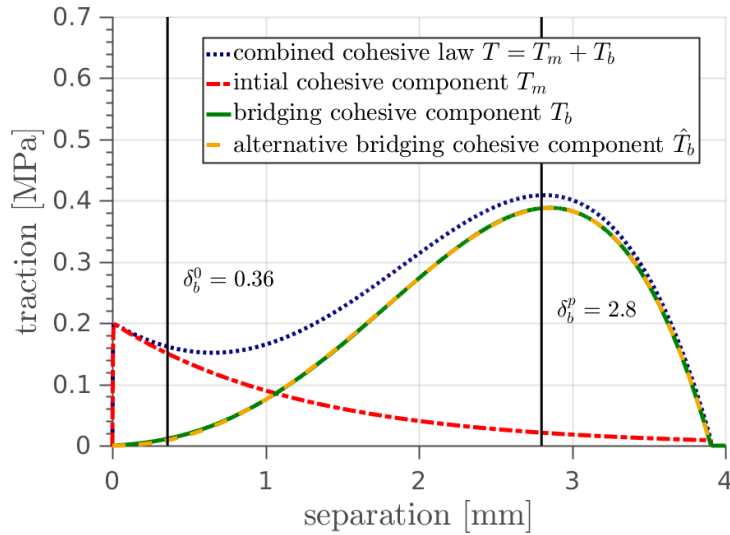


Figure 1: Overview of the proposed contributions to the total constitutive law. A summary of all used parameters is given in Table 2 and several characteristic numerical values of the law are given in Table 3.

of possible positions of the crack tip, depending on the criterion, range between a_{max} and a_{min} and $l_{PZ} = a_{max} - a_{min}$ holds.

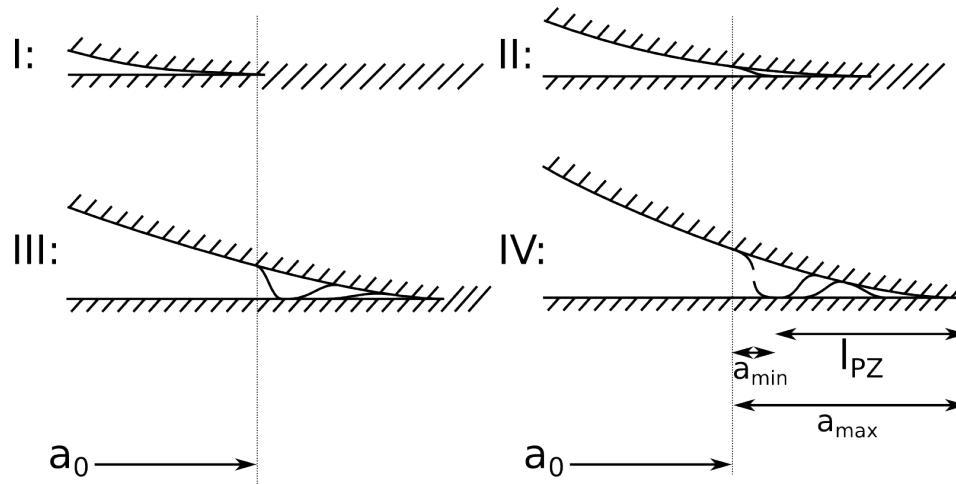


Figure 2: The four stages of interfacial failure in a honeycomb sandwich panel exhibiting fiber bridging. Stage I: unbridged interface crack is forming. Stage II: the unbridged crack propagates and fiber bridging initiates. Stage III: propagation of unbridged crack is slowed while bridging fully develops. Stage IV: the bridging zone is fully formed and both crack types propagate self-similarly.

The initial cohesive component, which is related to interface fracture, is governed

by

$$T_m(\delta_n) = \begin{cases} \delta_n/\delta_m^0 T_m^{max}, & \text{for } \delta_n < \delta_m^0 \\ T_m^{max} e^{-\alpha (\delta_n/\delta_m^0 - 1)}, & \text{for } \delta_m^0 \leq \delta_n \leq \delta_b^f \\ 0, & \text{for } \delta_b^f < \delta_n \end{cases} \quad (2)$$

where T_m^{max} is the maximum normal matrix/interface traction, δ_m^0 is the separation at which damage initiation starts in the matrix, and α is directly evaluated through the CERR as

$$\alpha = \frac{1}{\frac{G_{Ic,m}}{T_m^{max} \delta_m^0} - \frac{2}{3}} \quad (3)$$

The specific constant pre-peak penalty stiffness / exponential softening formulation used here is based on [21, 22], where the formulation was proposed for modeling of mode II delamination behavior. After considering several existing cohesive laws to represent the unbridged behavior, it was found that the smooth post-peak behavior yielded good results in this work.

The modeling of the bridging component is more challenging. The existing approaches are usually based on either a tri-linear [13, 16, 18], a square root [20] or an exponential [49] cohesive law. In these cases the laws have a very sharp peak and a subsequent steep drop, which leads to monotonically decreasing tractions in the wake of the crack tip. However, this was not observed in the current study. The maximum principal strain pattern of the fully developed SCB cohesive bridging zone obtained via DIC is shown in Figure 3. This corresponds to stage IV in Figure 2. The regularly spaced vertical high strain regions are associated with the honeycomb cell walls. It can be seen that there is a strain intensification around the crack tip. In the wake of the crack tip the strain values decrease in the zone where the initial interface crack has already occurred but the fiber rotation has not yet occurred. Further back along the wake of the crack, the fibers have already rotated and are sufficiently aligned in loading direction. Thus, the strain increases again to at least the initial crack tip level or possibly higher. A short distance further away from the second bridging-related peak the strains tend to 0, indicating a traction-free surface. The two aforementioned zones are separated by a transition zone with relatively low strain. The observed behavior in this honeycomb core sandwich application is distinct from observations made in solid laminate experiments, cf. [49]. There is a third region with distinct tensile strain, labeled region R in Figure 3. The strain in this region does not extend all the way to the facesheet, but occurs in the center of the sandwich core. It is still unclear what causes the strain pattern. Possible explanations include the oblique crack growth, that was observed during this particular experiment or thumbnail-shaped crack growth, which is commonly reported in the case of solid laminates [50–52].

In order to address the observed bridging behavior numerically, a new cohesive law shape which accounts for the observed bridging behavior is proposed and denoted by the index b . It reflects the observation that fibers in the bridging zone in the honeycomb panel specimens tend to undergo a rotation and stretching process after a macroscopic interfacial crack has developed. Once the fibers are sufficiently aligned

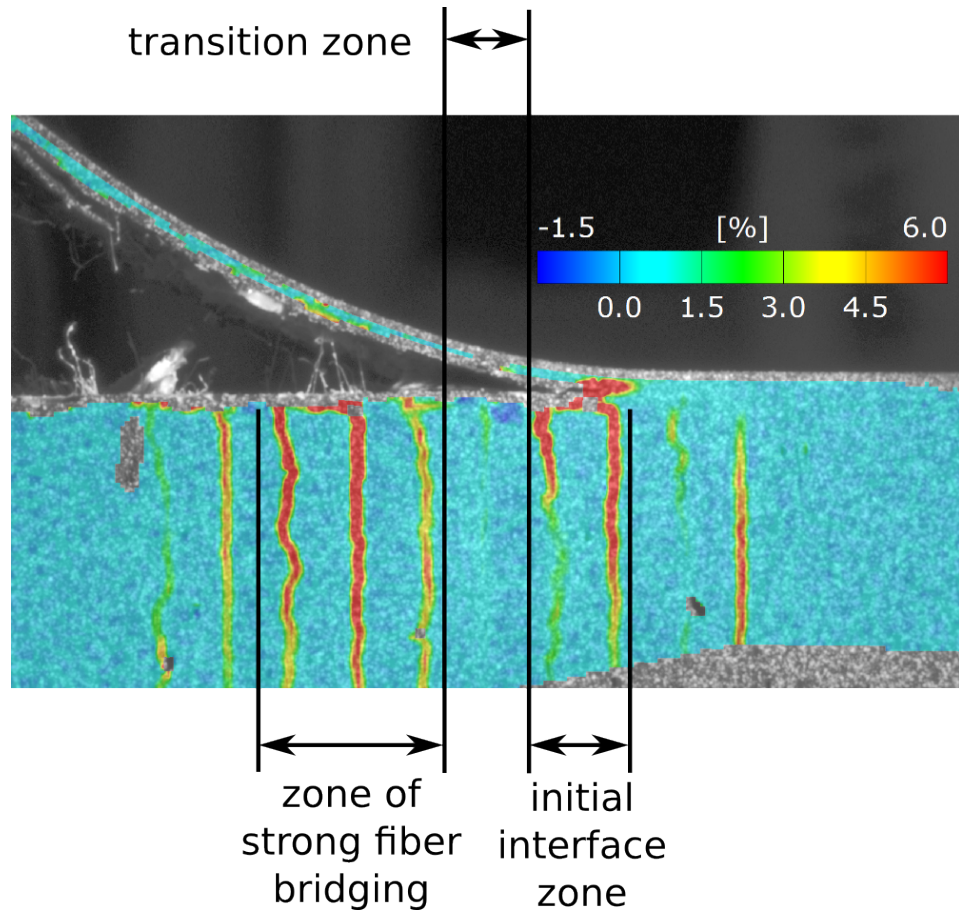


Figure 3: Maximum principal strain pattern of the SCB obtained through DIC.

with the load direction, traction is transferred by these fibers across the crack. The transferred traction increases until the filament debonds further and ultimately separates. This part of the cohesive behavior is referred to as the bridging cohesive component which leads to the traction T_b .

2.2 Proposed bridging cohesive component - with nonzero stiffness in the origin

A cohesive relationship that satisfies the described behavior of the bridging part, in the case of monotonic loading, is

$$T_b(\delta_n) = \begin{cases} 0, & \text{for } \delta_n < 0 \\ C_b \left[\left(\underbrace{\frac{\delta_n}{\delta_b^p}}_{(a)} + \underbrace{\frac{\delta_b^0}{\delta_b^p}}_{(b)} \right)^q - \left(\underbrace{\frac{\delta_n}{\delta_b^p}}_{(c)} \right)^{q+r} - \left(\underbrace{\frac{\delta_b^0}{\delta_b^p}}_{(d)} \right)^q \right], & \text{for } 0 \leq \delta_n \leq \delta_b^f \quad (4) \\ 0, & \text{for } \delta_b^f < \delta_n \end{cases}$$

where q and r are positive numbers, δ_n is the separation, and C_b , δ_b^0 , and δ_b^p (all greater 0) are model parameters. δ_b^f is the separation at total failure and is not an independent parameter itself, but can be calculated from δ_b^0 and δ_b^p , as described in [A](#). In Eq. (4) part (a) dominates the pre-peak section of the traction curve, whereas part (c) dominates the post-peak section of the curve. Equation (4) part (b) accounts for an initial non-zero slope and part (d) ensures that a zero separation is associated with a zero traction. As δ_n^0 tends to 0, the value of δ_b^p tends to the failure separation. However, for reasonable parameter choices, δ_b^p is approximately the separation at the traction peak of the combined cohesive law T_c . In the present investigation $q = 3$ and $r = 1$ were found to provide close agreement with experimental observations. All numerical results are therefore based on this choice for the exponents. The influence of various specific parameter choices on the traction-separation curves, as well as the SCB load-displacement behavior are plotted and discussed in [Section 6](#). The traction-separation response resulting from the described mechanisms is plotted in [Figure 1](#). It is noteworthy that the traction values are two orders of magnitude lower than the established literature values for solid laminate carbon fiber reinforced composite (CFRP) delamination ($T^{max} \approx 60 \text{ MPa}$). The lower magnitude is due to the fact that, in this work, honeycomb sandwiches are investigated and a continuum representation for the honeycomb structure is chosen. The relatively high stresses at the walls of the honeycomb in the physical specimens are smeared out over the entire cross section of the cell in the continuum model, and comparatively low tractions are the result.

Irrespective of the specific choice of T_b , the CERR of the bridging component can generally be calculated through

$$G_{Ic,b} = \int_0^{\delta_b^f} T_b(\delta_n) d\delta_n \quad (5)$$

The total CERR is thus

$$G_{Ic} = G_{Ic,m} + G_{Ic,b} \quad (6)$$

2.3 Proposed alternative bridging cohesive component - with zero stiffness in the origin

The formulation proposed in Section 2.2 has the advantage of having a positive stiffness in the origin, i.e.

$$\lim_{\delta_n \rightarrow 0^+} \frac{\partial T_b}{\partial \delta_n} > 0 \quad (7)$$

This means that $T_c = T_b$ with $T_m = 0$ is well-defined and that T_b can be investigated separately, i.e. without an additional component T_m . However, the mathematical form is somewhat impractical. Especially term (b) of Eq. (4) makes it rather difficult to find general solutions for e.g. the separation at failure, or the separation at the highest traction for general parameters q and r . Therefore, a simplified version of the bridging cohesive component \hat{T}_b with $\delta_b^0 = 0$ is proposed, which simplifies the calculation of these quantities substantially, as shown in Section 2.4. The proposed form for \hat{T}_b is

$$\hat{T}_b(\delta_n) = \begin{cases} 0, & \text{for } \delta_n < 0 \\ \hat{C}_b \left[\left(\frac{\delta_n}{\hat{\delta}_b^f} \right)^{\hat{q}} - \left(\frac{\delta_n}{\hat{\delta}_b^f} \right)^{\hat{q}+\hat{r}} \right], & \text{for } 0 \leq \delta_n \leq \hat{\delta}_b^f \\ 0, & \text{for } \hat{\delta}_b^f < \delta_n \end{cases} \quad (8)$$

\hat{T}_b depends only on the separation at total decohesion $\hat{\delta}_b^f$, the scaling parameter \hat{C}_b and the exponents \hat{q} and \hat{r} . As shown in Figure 1, the parameters can be chosen such that T_b and \hat{T}_b yield nearly identical results except for the immediate vicinity of the origin. The parameters, which were obtained by least square optimization in Matlab, are given in Table 2. \hat{T}_b has no stiffness in the origin

$$\lim_{\delta_n \rightarrow 0^+} \frac{\partial \hat{T}_b}{\partial \delta_n} = 0 \quad (9)$$

for $\hat{q} > 1$ and $\hat{r} > 0$, and should therefore only be used without a nonzero T_m component.

2.4 Parameter identification

The parameters of the cohesive law in Table 2 are for the most part not directly physical in the sense that they can be obtained from experimental data without further calculations. However, the shape of the cohesive law can be linked directly to experimental data. Figure 4 shows a number of chosen separation values, which can be directly related to the traction-separation plot in Figure 1. Characteristic points include 1.) the separation at which the combined cohesive traction assumes the lowest value between the two traction peaks (delta 1), 2.) the separation at which the cohesive traction peak is reached (delta 2) 3.) and the separation which is associated with a completely failed interface (delta 4). These values can be used to determine the values δ_b^0 , δ_b^p for T_b , i.e. the parameters which control the general shape of the cohesive bridging component (q and r assumed constant) up to a

scaling constant C_b . Analogously $\hat{\delta}_b^f$, \hat{q} , and \hat{r} can be derived for \hat{T}_b and the scaling parameter \hat{C}_b remains. Furthermore, there are a number of quantities which are not

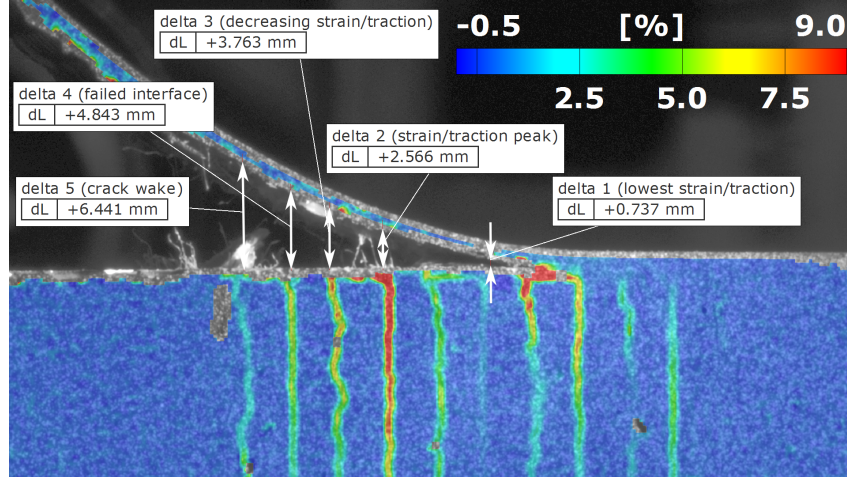


Figure 4: DIC principal strain plot with characteristic separations.

Table 1: Analytical expressions which relate characteristic quantities like the stiffness in the origin or the fracture toughness to parameters of the cohesive law.

	T_b	\hat{T}_b
separation at highest traction	$\approx \delta_b^p$	$\hat{\delta}_b^f \left(\frac{\hat{q}}{\hat{q} + \hat{r}} \right)^{1/\hat{r}}$
highest traction value	see A	$\hat{C}_b \left(\left(\frac{\hat{q}}{\hat{q} + \hat{r}} \right)^{\hat{q}/\hat{r}} - \left(\frac{\hat{q}}{\hat{q} + \hat{r}} \right)^{(\hat{q} + \hat{r})/\hat{r}} \right)$
failure separation	see A	$\hat{\delta}_b^f$
stiffness in the origin	$C_b q \frac{(\delta_b^0)^{(q-1)}}{(\delta_b^p)^q}$	0
CEER	see A	$\frac{\hat{C}_b \hat{\delta}_b^f \hat{r}}{(\hat{q} + 1)(\hat{q} + \hat{r} + 1)}$

Table 2: Cohesive parameters used in Figure 1.

initial/matrix component			bridging component				
[MPa]	[J/m ²]	[mm]	[MPa]	[mm]	[mm]	[-]	[-]
$T_m^{max} = 0.2$	$G_{Ic} = 250$	$\delta_m^0 = 0.005$	$C_b = 0.95$	$\delta_b^0 = 0.36$	$\delta_b^p = 3.0$	$(q = 3)$	$(r = 1)$
			$\hat{C}_b = 1.378$	-	$\hat{\delta}_b^f = 3.904$	$\hat{q} = 2.111$	$\hat{r} = 2.516$

directly input parameters, but derived values, calculated e.g. through Table 1. The benefits of the alternative bridging component become quite apparent in this table. On the one hand, all the characteristic quantities related to \hat{T}_b depend linearly on

\hat{C}_b and/or $\hat{\delta}_b^f$ and a factor which depends on the power parameters \hat{q} and \hat{r} . On the other hand, the characteristic quantities related to T_b are more complex, depend on the modeling parameters δ_b^0 and δ_b^p in a non-linear way and the evaluation can be rather complicated for arbitrary powers q and r , see A. As described in some detail

Table 3: Characteristic quantities associated with the used cohesive laws. Cohesive input parameters are shown without parenthesis and derived parameters are in parenthesis.

	T_m	T_b	\hat{T}_b	T_c / \hat{T}_c
separation at lowest inter-peak traction [mm]	-	-	-	(0.66)
separation at highest traction [mm]	0.005	2.85	2.85	(2.8)
highest traction value [MPa]	0.2	(0.388)	(0.388)	(0.409)
failure separation [mm]	(3.9)	(3.906)	3.904	(3.906) / 3.904
stiffness in the origin [MPa/mm]	(40)	(0.0137)	(0)	(40.0137) / (40.0)
CERR [J/m^2]	250	(774)	(778)	(1024) / (1028)

in Section 6, the load-displacement curve at displacement values which significantly exceed the displacement associated with the peak-load are only a function of the total CERR. Thus, this part of the load-displacement curve can be used to determine the scaling parameters such that the correct CERR is achieved. The only remaining question is then how the total CERR $G_{Ic} = G_{Ic,m} + G_{Ic,b}$ should be split up between the two components. In the present study the authors chose the parameters C_b , \hat{C}_b (and thus implicitly $G_{Ic,b}$) as well as T_m^{max} and $G_{Ic,m}$ such that the strain patterns of the FE calculations qualitatively agree with the strain distribution in the DIC measurements. This, for instance, resulted in a bridging cohesive strength which was almost twice as high as T_m^{max} and a ratio of $G_{Ic,b}/G_{Ic} = 774/1024 \approx 0.756$.

3 Experiment

3.1 Materials and manufacturing

A 609.6 mm by 609.6 mm honeycomb sandwich panel was manufactured from IM7/8552-1 prepreg tape and 49.66 kg/m^3 Hexcel 5052 aluminum honeycomb core with a 0.0178 mm foil gauge, 3.175 mm cell size, and a 25.4 mm height. Eight-ply facesheets were hand-laid with a $[45/90/-45/0]_s$ stacking sequence, with FM-300K film adhesive between the facesheets and core. To introduce the initial disbond between the core and the one facesheet, a 101.6 mm wide strip of Teflon was placed between the facesheet and the film adhesive at the middle of the panel along the entire 609.6 mm length in one direction. The panel was then bagged and co-cured in an autoclave following a standard pressure/temperature profile.

3.2 Single Cantilever Beam test

Currently no ASTM standard exists for measuring interfacial (facesheet-core interface) CERR of composite sandwich panels, as this is an active area of research [53,54]. One conclusion that can be drawn from the available literature is that the Single Cantilever Beam (SCB) currently provides the most viable means for measuring the interfacial CERR for composite sandwich panels. In this context the interface refers to a general area where the honeycomb core touches the facesheet and is bonded by an adhesive. This adhesive wicks up a portion of the honeycomb cells. ASTM Standard D 5528 [55] provides experimental procedures for measuring the interlaminar CERR for solid laminates using Double Cantilever Beam (DCB) and SCB specimens. SCB specimens were cut, in accordance with width and length dimensions provided in ASTM Standard D 5528 [55] for solid laminates, from the 609.6 mm by 609.6 mm honeycomb sandwich panel. A schematic of the specimens is shown with general load introduction in Figure 5, and a photograph of a specimen with load introduction through a loading block is shown in Figure 6. The specimens were 203.2 mm by 25.4 mm with a 27.94 mm height, which is comprised of the 25.4 mm core and the top and bottom facesheets (each with a thickness of 1.25 mm). The specimens were cut such that each specimen contained a Teflon insert of 50.8 mm length between one facesheet and the core, which prevented bonding in that region. The bottom facesheet was clamped to prevent motion in all directions, providing a simple yet effective means of securing the specimen. The top facesheet was loaded through a pinned aluminum block, which was bonded to the end of the top facesheet above the disbond region, see Figure 6. The block dimensions were 25.4 mm by 25.4 mm by 15.9 mm. The pin hole was centered in the block. As shown in Figure 6, on both sides of the specimen, the exposed honeycomb cells near the top facesheet were filled with drywall compound to aid in crack identification. One surface was then painted with a speckle pattern, and this side of the specimen was monitored with DIC. On the opposite side, the crack length was monitored with a travelling optical telescope.

The SCB testing was performed on a load frame under quasi-static displacement control at a rate of 0.42 mm/s up to 44.48 N and after this at a decreased rate of 0.021 mm/s. Samples were subjected to a single precracking load/unload cycle to ensure a sharp crack tip for the subsequent loading. During the precracking cycle the samples were loaded up to a line load displacement of approximately 25.4 mm, which resulted in crack growth of greater than 25.4 mm and a substantial load drop. Results of three tests on specimens designated as SCB1, SCB2, SCB3 are reported in Section 6.

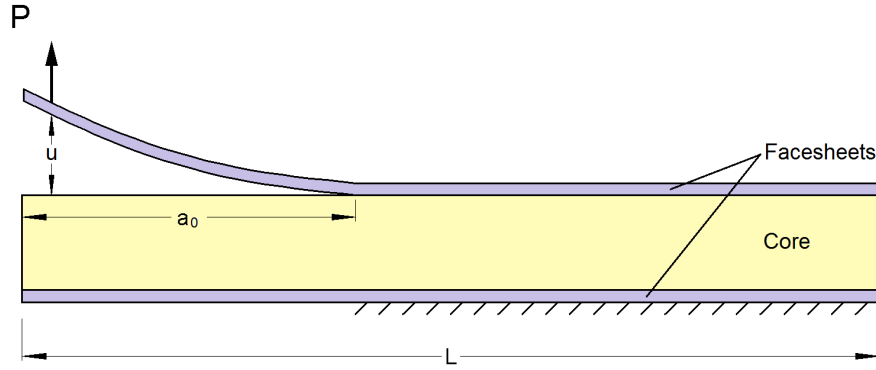


Figure 5: Schematic of the Single Cantilever Beam (SCB) setup.

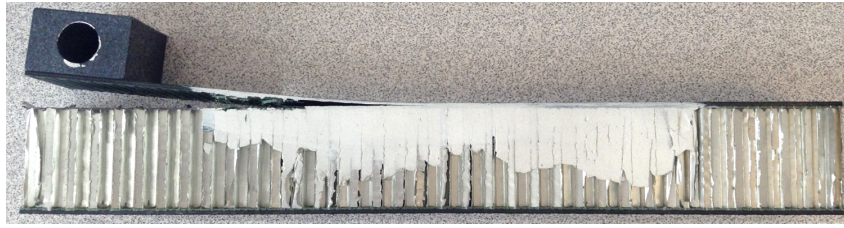


Figure 6: Photograph of a SCB specimen after testing.

4 Finite element implementation

The cohesive law described in Section 2 has been implemented in a 2D, zero thickness, traction-separation user element formulation as described, for instance, by Park and Paulino in [24].

The governing weak form is given as

$$\int_{\Omega} \delta \boldsymbol{\varepsilon} : \boldsymbol{\sigma} dV + \int_{\Gamma_c} \delta \boldsymbol{\delta} \cdot \mathbf{T}_c dS = \int_{\Gamma} \delta \mathbf{u} \cdot \mathbf{T}_{ext} dS \quad (10)$$

where Ω refers to the volume of the domain, Γ_c denotes the potential (initially internal) fracture surface and Γ denotes the external domain boundary. The strain is defined as $\boldsymbol{\varepsilon} = \nabla^{sym} \mathbf{u}$. By using the elasticity tensor \mathbf{C} , the stress $\boldsymbol{\sigma}$ is obtained through $\boldsymbol{\sigma} = \mathbf{C} : \boldsymbol{\varepsilon}$ and \mathbf{T}_{ext} is the external traction.

Using the differential operator \mathbf{B} , which links global displacements to local separations, the internal cohesive force vector \mathbf{f}_{coh} is given by

$$\mathbf{f}_{coh} = \int_{\Gamma_c} \mathbf{B}^T \mathbf{T}_c dS \quad (11)$$

which then gives rise to the element stiffness matrix

$$\mathbf{K}_{coh} = \frac{\partial \mathbf{f}_{coh}}{\partial \mathbf{u}} = \int_{\Gamma_c} \mathbf{B}^T \frac{\partial \mathbf{T}_c}{\partial \boldsymbol{\delta}} \mathbf{B} dS \quad (12)$$

In Eq. (12) $\boldsymbol{\delta}$ is a vector of the form $\boldsymbol{\delta} = (\delta_n, \delta_s)^T$ consisting of a normal and a shear component. However, in this work, only the normal component, δ_n , is used for the

calculation of cohesive tractions and only normal tractions, $\mathbf{T}_c = (T_n, T_s) = (T_c, 0)$ result. Furthermore, in this study only monotonic loading is considered. Therefore, no unloading condition has yet been defined.

5 Finite element model

The loading and boundary conditions imposed on the finite element model of the SCB specimen are shown in Figure 7. Nominal dimensions are given. Only the lower half of the load introduction fixture has to be modeled since the aluminum block is very rigid and the force is introduced at its center. The support on the right side is introduced since there is no shear component in the cohesive law. While shear stresses should be negligible at the interface of a mode I delamination test, the support is still necessary in order to prevent horizontal rigid body translations of the top facesheet. All necessary material parameters are given in Table 4.

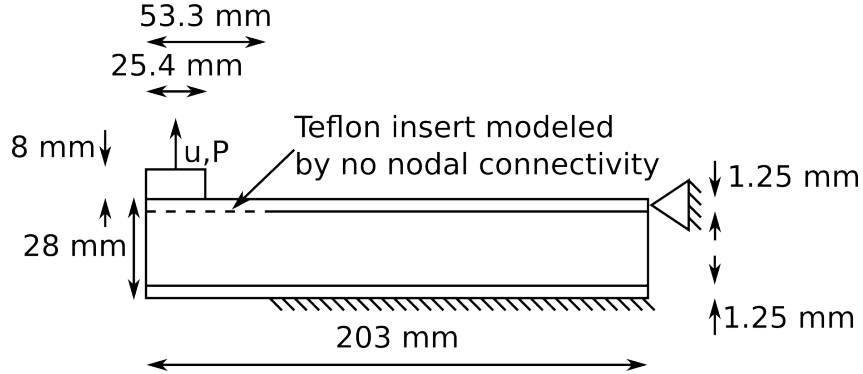


Figure 7: Schematic of the finite element model.

Table 4: Material parameters of the SCB.

facesheet		load introduction block			
[MPa]	[-]	[MPa]	[-]		
$E = 86593.9$	$\nu = 0.311$	$E = 72000$	$\nu = 0.3$		
core					
[MPa]	[MPa]	[-]	[-]	[MPa]	[MPa]
$E_{\parallel} = 517.1$	$E_{\perp} = 0.1467$	$\nu_{\perp\parallel} = 0.33$	$\nu_{\perp} = 0.0001$	$G_{\perp\parallel} = 151.68$	$G_{\perp} = 0.03669$

The quasi-isotropic facesheet has been modeled as isotropic. Isotropic material parameters were chosen to provide the correct lever compliance of the facesheet at a discretization of three elements in thickness direction, and an insert clearance of 0.1 mm was chosen. Since the stiffness of the laminate is orders of magnitude higher in any direction than the core stiffness and it is a 2D simulation, this choice does not

influence the results. The core was modeled as anisotropic due to the great disparity in Young's moduli in through-thickness and in-plane directions. For the facesheets, core and load introduction block Abaqus CPS4R reduced integration plane stress elements were used. The cohesive layer was modeled with cohesive user elements. A mesh refinement study was conducted in longitudinal direction to ensure sufficiently refined crack propagation results.

6 Results and discussion

The results and discussion section is split into four main parts. First, in Section 6.1 the performance of various existing cohesive zone formulations is compared to the experimental SCB load-displacement curves. Second, a comparison between the bridging component of the proposed cohesive law and the load-displacement curves of precracked specimens is made in Section 6.2. Third, both components of the proposed cohesive law are compared to the combined precracking and precracked load cycle in Section 6.3. Finally, the results of a sensitivity study with respect to mode mixity and other factors is presented.

6.1 Load-displacement results - existing formulations

First, a comparison of predictions by established cohesive formulations to experiments is presented. A bilinear approach as proposed in [11], an exponential softening approach according to [22], and a polynomial Park–Paulino–Roesler (PPR) approach as described in [24] are considered. The results are plotted in Figures 8-9. In order to avoid redundancy, only the parameter study of the bilinear law is discussed in detail in Figure 8, while only the best fit of the other formulations is presented in Figure 9.

Focusing on the bilinear traction-separation law [11], when the cohesive parameters were fitted to the experimental data, emphasis was placed on matching

1. the post-peak load-displacement curve
2. the peak load of the numerical predictions
3. the initial slope from the imposed precracking cycle

Concerning 1.) The load-displacement behavior at displacements much greater than at the peak load displacement is only governed by the value of the CERR, G_{Ic} , which is determined to be $G_{Ic} \approx 1050 \text{ KJ/m}^2$ in the current application. Bilinear cohesive laws are generally considered 2 parameter laws [56]. This leaves only one meaningful model parameter in the case of the bilinear cohesive law, which is the maximum traction. The maximum traction, T^{max} was varied systematically and the result is reported in Figure 8. The appropriate T^{max} -value, such that the numerically predicted peak load agrees with the experimental peak load, is $T^{max} = 0.5 \text{ MPa}$. Thus, requirement 2.) is fulfilled. The slope of the cohesive law before the maximum traction is mostly considered to be a nonphysical penalty stiffness [57]. However, there are several approaches of relating the penalty stiffness to material

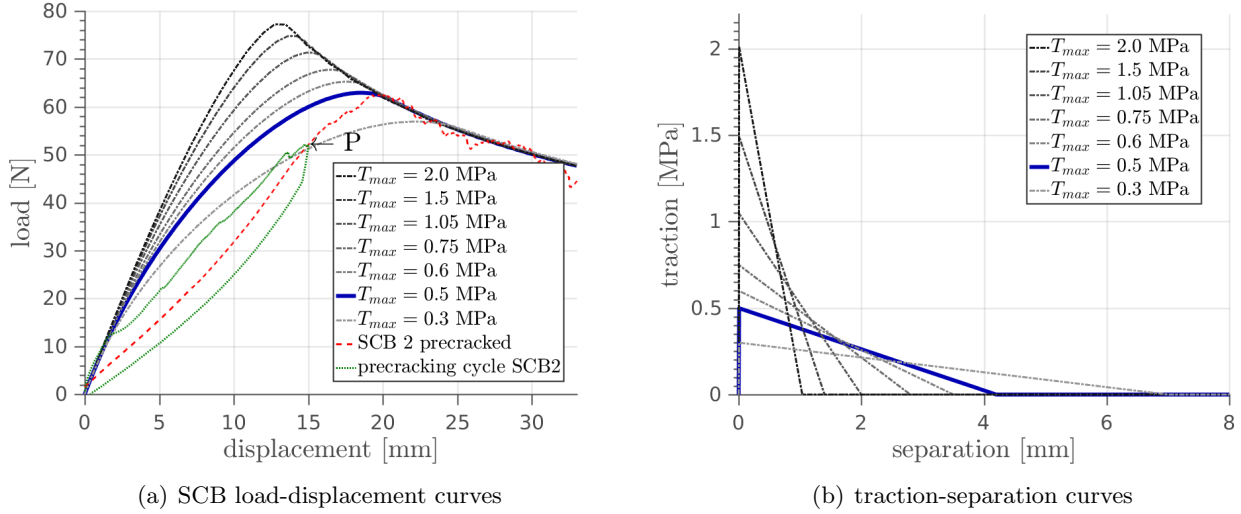


Figure 8: Parameter study of the bilinear cohesive formulation (COH2D4) for various T^{max} values. $G_{Ic} = 1050 \text{ KJ/m}^2$ in all cases.

parameters, cf. Turon et al. [25] and references therein. Since the area under the traction-separation curve is given by the CERR, the bilinear law is completely defined.

As expected, the variation of the penalty stiffness within reasonable bounds had no effect on the load-displacement curve. All parameters are reported in Table B1. The fulfilment of requirement 3.) is thus not linked to the penalty stiffness, but rather to the proper model geometry, elastic material parameters and boundary conditions. As the numerical predictions were in good agreement with the uncracked part of the experimental curve (initial part of the precracking cycle, green dashed curve) for all parameters, requirement 3.) has been met.

When overpredicted, the peak loads of the numerical prediction tend to be at smaller separations than the experimental results. This tendency decreases as the maximum traction is decreased. At the correct peak load value, the corresponding displacement is still slightly smaller than the experimentally observed value. If the peak load is significantly underpredicted, the peak load displacement is overpredicted for the bilinear cohesive law (Figure 8(a)).

The formulation with exponential softening behaves qualitatively similar to the bilinear formulation, as shown in Figure 9(b). Due to the upward concave shape of the post-peak traction-separation curve, the appropriate peak load value is found at a greater maximum traction compared to the bilinear formulation. In the bilinear, as well as in the exponential case, the T^{max} -value that provides the best fit transfers tractions from the facesheet to the core up to approximately 4 mm of separation.

The PPR model has a concave downward pre-peak / concave upward post-peak traction-separation curve shape, see Figure 9(b). The peak load is met at a maximum traction of 0.53 MPa which is between the best fit values of the exponential and bilinear law. This is plausible, as the convex post-peak curve is slightly less

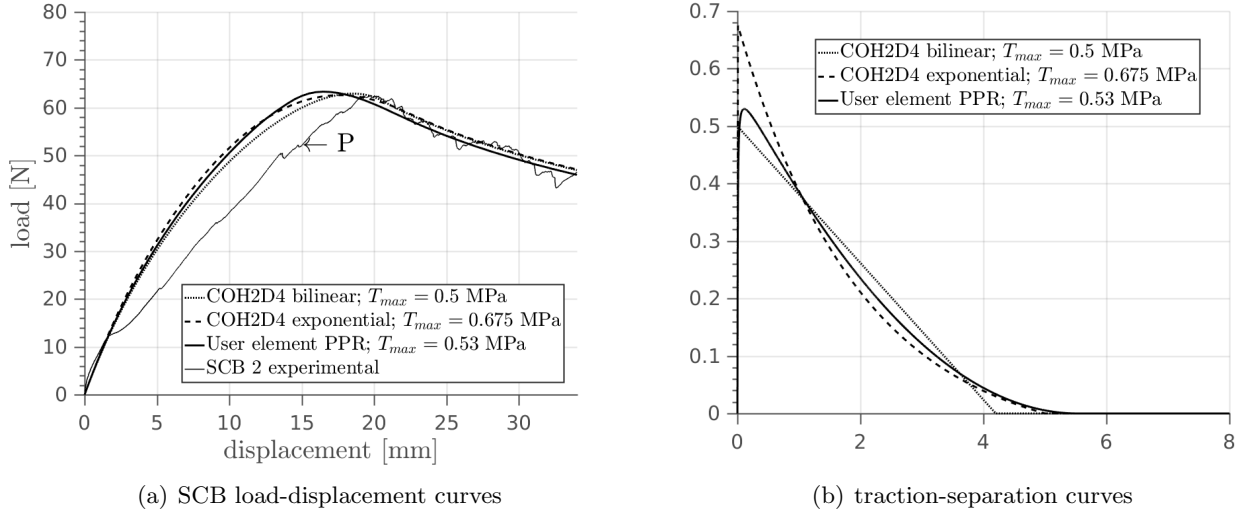


Figure 9: A comparison of the best fits obtained with the Abaqus COH2D4 bilinear, COH2D4 exponential and PPR model according to [24] to experimental data. $G_{Ic} = 1050 \text{ KJ/m}^2$ in all cases. The precracking and reloading cycle have been merged at point P.

pronounced than in the exponential case. The concave downward pre-peak shape of the traction-separation shifts the maximum load to larger displacements compared to the other laws. It also leads to a similar separation at total failure as the exponential formulation, despite slightly lower post-peak convexity. The formulation was examined in order to determine if a pre-peak behavior other than the traditional very high penalty stiffness provides a better fit to the experimental data. However, there is no substantial effect on the load-displacement curves, and the observations that were made for the bilinear and exponential law also hold for the PPR law.

While the goal of calibrating the cohesive zone input parameters to match the initial slope and the peak value was accomplished, the existing cohesive formulations show considerable deviations from the experimental data for significant parts of the curve, especially in the transition regime between the starting of the initial failure mechanisms and the fully formed fiber bridging zone. Furthermore, the slope of the numerical pre-peak predictions obtained with these methods are concave downward, whereas the experimental pre-peak results are concave downward / concave upward in the pre-peak part of the curve. In conclusion, all the investigated existing formulations are in very good mutual agreement, but not in good agreement with the experimental results.

All parameters for the respective best fits are provided in Table B2 in B. Due to the honeycomb structure of the core, the homogenized tractions in the z-direction are relatively low while, due to fiber bridging, the CERR values tend to be even higher than in solid laminate composites. The combination of low strength and high CERR leads to a pronounced dependence of the peak load on the strength, which is not observed in other studies [25], where reducing the cohesive strength is

even identified as a strategy to enable the use of coarser cohesive meshes without changing the structural load response. The reason for the observed behavior is the relatively high length of the process zone l_{PZ} which typically estimated as

$$l_{PE} = ME \frac{G_{Ic}}{(T^{max})^2} \quad (13)$$

cf. [16, 58], where E is the appropriate Young's modulus and M is a parameter that varies between 0.21 and 1.0, depending on the specific model. In most CFRP applications, T^{max} and G_{Ic} vary between e.g. 60 MPa and $G_{Ic} = 352 \text{ J/m}^2$ [25] and 2.326 MPa at $G_{Ic} = 100 \dots 180 \text{ J/m}^2$ [16]. This means that in the current application, the numerator of Eq. (13) is considerably lower ($T^{max} = 0.409 \dots 0.675 \text{ MPa}$) and the denominator is much higher ($G_{Ic} \approx 1000 \text{ J/m}^2$). Hence, the process zone must be relatively long, linear elastic fracture mechanics assumptions are violated and the peak load, as well as the load-displacement curve in general, depends much more strongly on the cohesive strength values than usually reported.

6.2 Load-displacement results - bridging component

In this section, a parametric study of the bridging contribution, T_b , of the proposed cohesive law is presented. The additive nature of the proposed cohesive law is quite suitable for a separate examination of the bridging component in absence of the initial cohesive component. To this end, T_m is set to 0 in this section, see Eq. (1), and the three independent parameters, as described in Section 2, are varied. The influence of each parameter is shown for the SCB load-displacement curves as well as for the traction-separation law in Figures 10-12.

A higher/lower value of δ_b^0 increases/decreases the failure strain and the maximum traction. An increase/decrease in δ_b^p leads to substantially higher/lower ultimate failure separations and lower/higher peak loads and tractions. Lastly, an increase/decrease of C_b stretches the entire traction-separation curve vertically and increases/decreases strength and toughness linearly. Clearly, these three parameters provide a good deal of flexibility to the model for fitting to experimental data.

The numerical results obtained when only accounting for the bridging component T_b of the proposed cohesive law can also be compared to the load-displacement curves obtained from precracked specimens. This comparison is justified if the matrix-related fracture energy G_m is much smaller than the bridging-related fracture energy G_b . This can be expected to be the case for precracked specimens once a certain crack opening has been exceeded and the fibers have rotated and can transfer traction across the interface. Conversely, this assumption is not expected to hold for non-precracked specimens, and during the rotation process, when the contribution of T_m is still significant.

Figures 10, 11 and 12 illustrate the effects of varying parameters δ_b^0 , δ_b^p , and C_b , respectively, on the bridging cohesive model's prediction of the SCB load-displacement behavior and the traction-separation behavior at the facesheet/core interface.

Since there is some scatter in the experimental results, it is next demonstrated that the proposed bridging part of the cohesive model can match the response of each SCB specimen, after the precracking load cycle. As shown in Figure 13, the

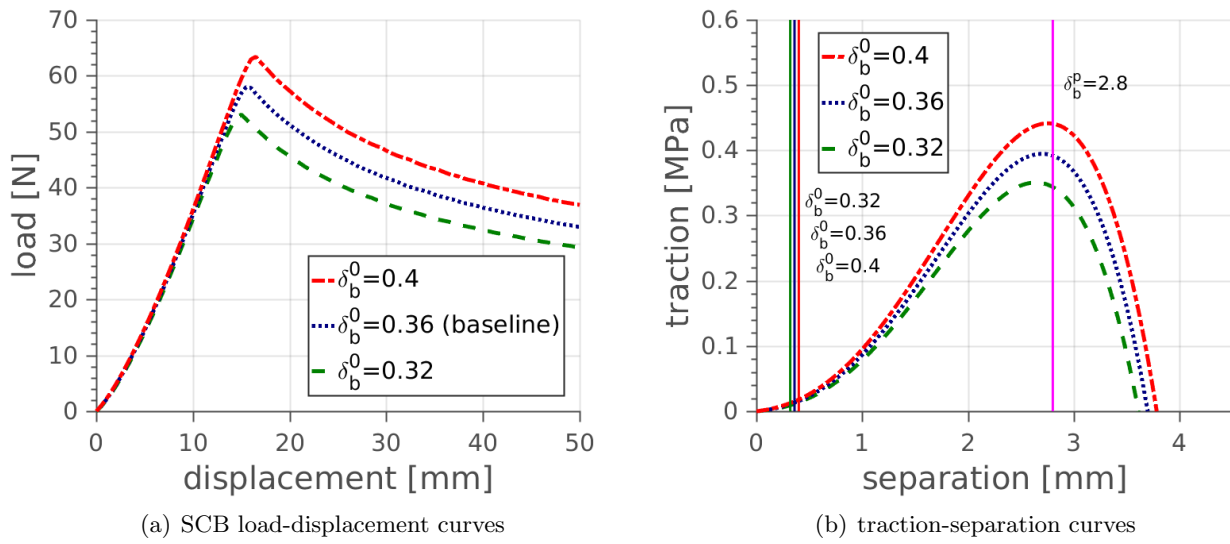


Figure 10: Effect of the variation of δ_b^0 . The vertical green, blue and red lines mark the values of the varied parameter δ_b^0 while the magenta line indicates the parameter δ_b^p , which is held constant in this figure.

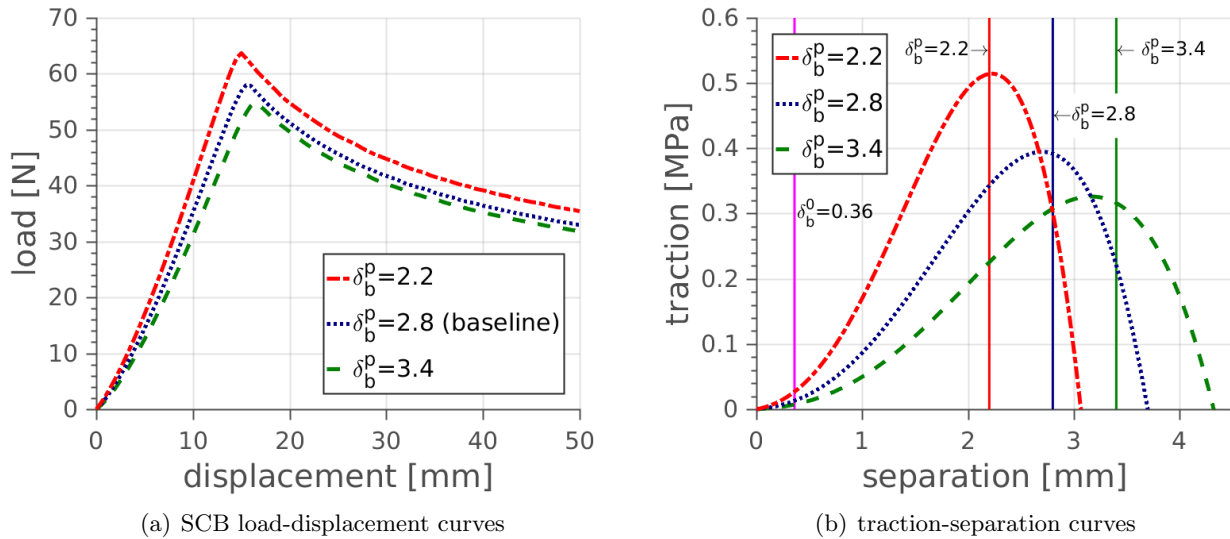


Figure 11: Effect of the variation of δ_b^p . The vertical green, blue and red lines mark the values of the varied parameter δ_b^p while the magenta line indicates the parameter δ_b^0 , which is held constant in this figure.

proposed cohesive law is able to provide a very good fit to each of the three SCB experimental result load-displacement curves. The required parameters are shown in Table 5. While there is some scatter in the experiments, the level of scatter is

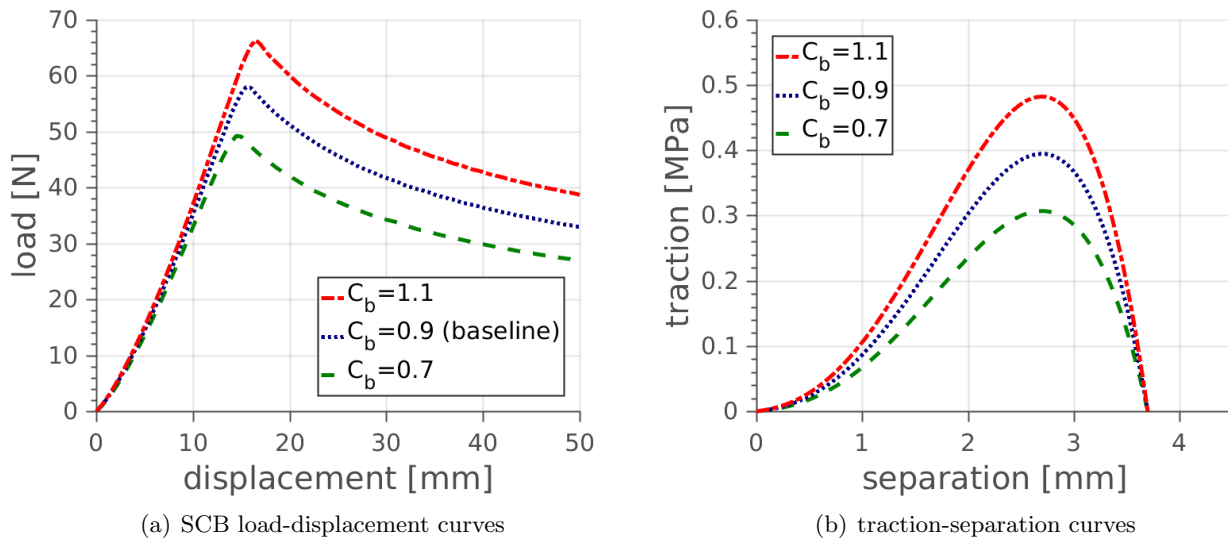


Figure 12: Effect of the variation of C_b .

Table 5: Parameters used in Figure 13.

SCB no.	C_b [MPa]	δ_b^0 [mm]	δ_b^p [mm]	q [-]	r [-]
1	1.65	0.2	2.3	3	1
2	1.2	0.36	3.75	3	1
3	0.905	0.36	3.0	3	1

fairly low compared to other fiber bridging investigations [33, 41].

It is of particular interest that the obtained numerical load-displacement curves are convex in the pre-peak regime, as are the experimental curves, unlike the load-displacement curves of the existing formulations shown in Section 6.1. The post-peak curve is also captured very well in a mean sense. The local load drops present in the experimental curve result from breaking bridging fiber bundles and obviously cannot be captured by cohesive elements with uniform properties. However, this is not an issue since the failing is assumed to be stochastic, varying from test to test, and thus the simulated curves represent only the mean values. At this point no additional analysis or design insight is expected from the resolution of the load drops in a stochastic sense. There is some slight deviation between the experimental and simulated curves during the initial 5 mm of displacement, which is attributed to the fact that the initial cohesive component is neglected. As will be shown in Section 6.3, this can be addressed by adding the initial cohesive component to the formulation.

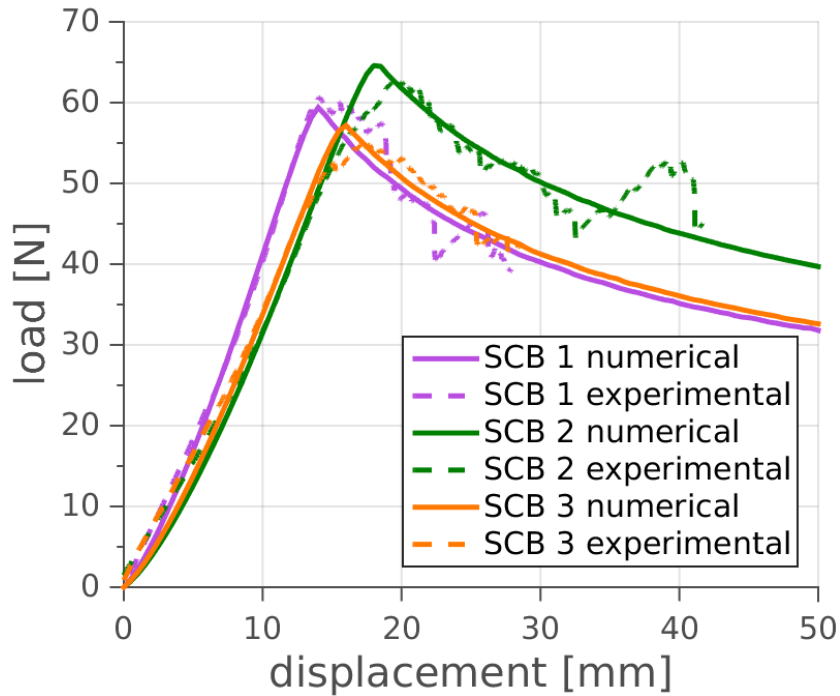


Figure 13: Comparison of numerical results obtained with only the bridging part of the new cohesive formulation and experimental results of precracked specimen.

6.3 Load-displacement results - combined law

The following discussion of the results of the combined cohesive law is limited to correlation with specimen SCB 2. The specimen was experimentally precracked by applying a loading point displacement of approximately 15 mm. Subsequently the specimens was unloaded to zero traction and reloaded. As shown in Figure 14, there is no significant in-plane damage accumulation during the unloading and reloading. This can be concluded from the fact that, on reloading, the curve goes through point P again (see Figure 8(a)), which is the maximum loading point during the precracking procedure. However, the unloading and loading curves are not identical. This is caused by the bridging fiber bundles, which lose the majority of their traction even after a very slight reduction in loading point displacement.

Since the loading/unloading case distinction is not considered in this work, monotonic loading is assumed in the numerical model. Therefore, the numerical curve should follow the precracking curve up to point P and subsequently follow the reloading curve. The results obtained using the combined cohesive law (Eq. (1)-(4), Figure 1) with the parameter set listed in Table 2 are shown in Figure 14.

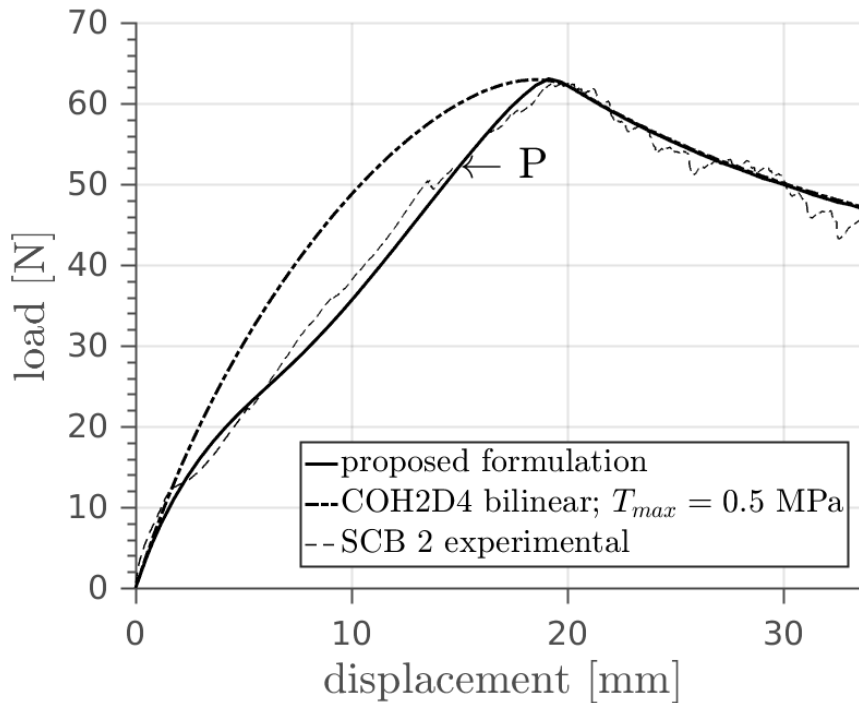


Figure 14: Comparison of a simulation using the cohesive law depicted in Figure 1 to experimental data. The experimental precracking curve has been merged with the reloading curve in point P.

By selecting the appropriate parameters, the combined law is in very good agreement with the precracking cycle prior to point P, as well as with the subsequent loading cycle for displacements greater than 15 mm. The initial matrix cracking and the subsequent forming of a bridging zone, indicated by the concave downward / concave upward load-displacement curve transition, is also clearly captured. The simulated strain contour plots are compared to experimental DIC-strain measurements in Figure 15. The x-direction edge length of the elements in Figure 15 is approximately 1 mm. In Figure 15 a), the specimen is shown before the initiation of damage, during the precracking cycle. The initial high strain between the facesheet and the core in this figure is caused by the Teflon insert. This is indicated by the fact that the core is still practically strain-free. As the loading point displacement is increased, the initial interfacial disbond forms, see Figure 15 b). The subsequent forming of the bridging cohesive zone, with the substantial bridging zone, is shown in Figure 15 c). In Figure 15 d) both the numerical and the experimental strain plots indicate two zones of strain concentration. One is interface-related, at relatively small separations, and the other is bridging-related, at a separation of several mm. At this point, the bridging zone is fully developed. A further increase in loading point displacement leads to a self-similar propagation of the crack. This is indicated by Figures 15 d) and 15 e), which look very similar, except that the crack has propagated one cell length to the right. The 4 stages in Figure 15 correspond

to the 4 stages identified in Figure 2.

To assess the computational performance of the proposed combined cohesive law,

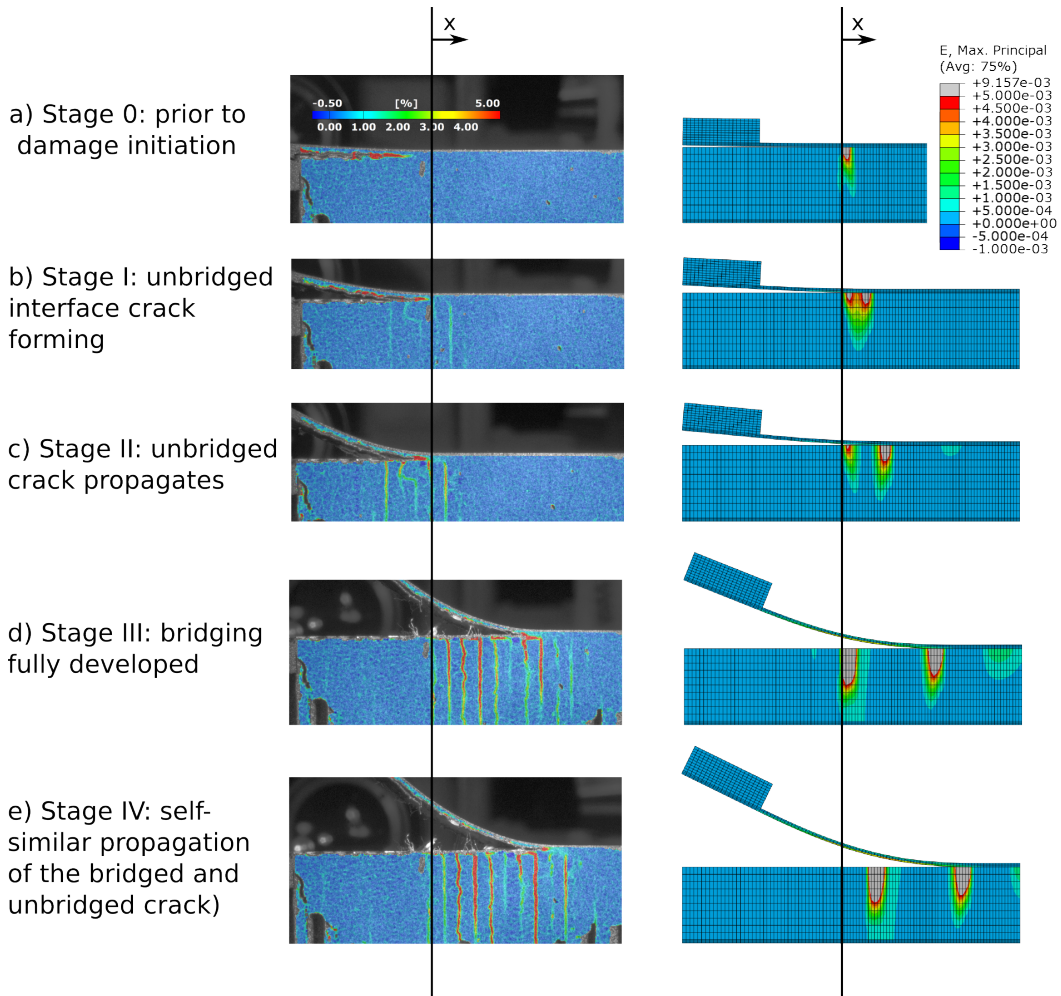


Figure 15: Comparison of the experimental SCB 2 results (left) and the numerical predictions (right) for the 4 stages of crack growth.

a comparison has to be made to the performance of existing formulations examined in Section 6.1. The wall-clock time, average iterations per converged increment (AIPCI) and number of unconverged iterations are compared in Table 6. All calculations were conducted with the arc length method and identical solution and control parameters. The parameters were chosen such that a displacement of 60 mm would be accomplished in approximately 120 increments in order to obtain sufficiently detailed force-displacement plots. The wall-clock time is measured from the starting of the job in Abaqus 6.14 interactive mode until the completion and hence includes all the time required for initialization and finalization of the calculation. The employed computer system is a Dell Precision M4800 with Intel Core i7-4810MQ and 32GB RAM, and only one thread was used simultaneously. Table 6 clearly shows that the cohesive formulation proposed in this paper has the best numerical performance of

Table 6: Comparison of numerical efforts.

Formulation	# converged increments [-]	wall-clock time [s]	AIPCI [-]	# unconverged increments [-]
new formulation	123	43.3	2.650	0
COH2D4 bilinear	126	140.3	7.103	33
COH2D4 exponential	126	138.7	7.140	32
PPR	126	60.6	3.794	1

the investigated formulations, although the shape of the cohesive law is more complex than the other investigated laws. This emphasizes that the additional modeling complexity does not lead to an increased computational effort and that the proposed formulation is at least as suitable as established formulations for systems with many degrees of freedom, such as large structures. The second most efficient formulation is the PPR formulation. The PPR formulation is only slightly less convergent than the proposed formulation, requiring approximately 40% more wall-clock time and 2.4% more total converged increments. The difference in wall-clock time is mostly caused by a slightly higher AIPCI. There is a notable difference between the two aforementioned formulations and the two considered Abaqus COH2D4 element formulations, which require more than twice as much wall-clock time, a much higher number of unconverged iterations, and a higher AIPCI. The data presented in Figures 9 and

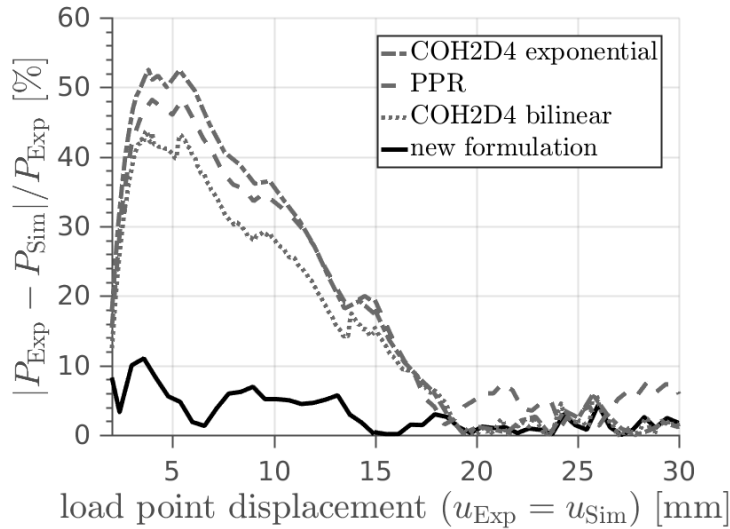


Figure 16: Relative deviation of predicted load (Sim.) and measured load (Exp.) for various formulations.

14 is recomputed in order to yield the relative deviation between the predicted and measured load values at a given displacement, see Figure 16. The relative load devi-

ation of the newly proposed formulation is generally below 10% whereas the relative deviation of the reference formulations tends to be substantially higher. For the previously stated reasons, the difference decreases, as the crack length increases.

6.4 Mode mixity and geometric nonlinearity

The general treatment of the mode mixity - especially between mode I and II (cf. Davidson et al. [59], and Park and Paulino [60] and Sørensen and Kirkegaard [61]) - and specifically the mode mixity of delamination characterization tests, cf. Reeder and Rews [62], receive substantial attention in the scientific community. While a number of mixed-mode formulations are available, it has recently been pointed out, that many formulations, potential-based as well as non-potential-based, exhibit difficulties in accurately capturing the crack propagation condition [59]. The crack in a symmetric DCB which is loaded by pure bending moments propagates under pure mode I [20]. However, this is generally not the case for SCB specimens, as the neutral axis is not aligned with the crack plane [63]. This holds for most specimen geometries intended for the interface testing of sandwich panels like the Three-Point-Bend Sandwich / Single Leg Bend specimen [40, 59], Tilted Sandwich Beam, Modified Cracked Sandwich Beam [64] etc. A further complication is that the mode mixity tends to change as the crack grows. Generally, cracks start with a relatively high mode I contribution and the relative mode II contribution increases, as the crack propagates [40, 59]. However, if relatively pure mode loading is intended, the geometry can be chosen explicitly such that the interface coincides with the neutral axis, as Davidson et al. have recently shown [63].

In order to determine the effects of mode mixity, the artificial boundary condition on the right side of the top specimen, and nonlinear geometry specifically in the current investigation, an extensive simulation campaign has been conducted. This was accomplished by simulating all permutations of the traits

1. $T_c = (T_n, T_s)$ vs. $T_c = (T_n, 0)$
2. small deformations vs. finite deformations
3. plane stress vs. plane strain
4. artificial boundary condition at the top right vs. no artificial boundary condition at the top right (in the case of $T_c = (T_n, T_s)$)

For all possible permutations of the four traits, the load-displacement curve was virtually unaffected by whether T_c had a cohesive shear component or not. Therefore, setting the shear component to 0 is permissible in the current investigation. However, if the formulation is to be used in general applications, an extension to mixed-mode capabilities is mandatory. Furthermore, for the cases which had a cohesive shear component, the load-displacement curves with and without the artificial support were identical. Thus, introducing the support is permissible. Plane strain assumptions increase the predicted load by about 5% compared to plane stress assumptions at a given displacement. Preliminary investigations of 3D geometries

suggest that plane stress assumptions may be more appropriate for the considered specimen and thus all reported simulations were conducted under plane stress boundary conditions. Including the effects of geometric nonlinearity increased the predicted load by about 5% at a given displacement for the established formulations. As the effect is relatively small, the current analysis is limited to small displacement assumptions.

6.5 Engineering estimate of the apparent energy release rate

It has been frequently observed, that fiber bridging leads to an increase in energy release rate, cf. [40], [47] and references therein, and that the CERR increases over the crack length [65, 66]. However, the CERR should, by definition, be an interface property and not depend on the crack length. In order to address this discrepancy, we distinguish between a constant constitutive CERR, which is a material parameter and defined as the area under the traction-separation curve, Eq. (14),

$$G_{Ic,const} = \int_0^{\delta_b^f} T_c d\delta_n \quad (14)$$

and the experimentally observed apparent CERR, as defined by the load point displacement, load, and crack length at a given lever arm stiffness

$$G_{Ic,ASTM} = \frac{3Pu}{2b(a_0 + \Delta a)} \quad (15)$$

which is apparently not constant as it is subject to the R-curve effect etc.

In order to directly compare the R-curves that correspond to FE calculations to the R-curves calculated from experiments based on Eq. (15), a crack criterion for the FE calculation is needed. It is seldomly discussed how the apparent CERR can be directly extracted from an FE calculation since the constitutive CERR can easily be calculated as the area under the traction-separation curve. There are multiple possibilities for determining the crack length Δa . For instance:

1. Opening threshold; i.e. a relative displacement of the upper and lower surface
2. Strength reduction threshold
3. Dissipated energy threshold
4. Damage onset, or respectively, the traction peak
5. Compliance-based estimates

In the presence of a short process zone, the five stated options provide very similar results. The crack length enters $G_{Ic,ASTM}$ in the denominator as $a_0 + \Delta a$ (see Eq. (15)). However, the actually measured value is $a_0 + \Delta a + \hat{a}$, where \hat{a} is the difference between the “correct” Δa value and the Δa that the chosen crack criterion / experimental technique provides. $\Delta a + \hat{a}$ should fall in the range of $a_{min} < \Delta a + \hat{a} < a_{max}$ as defined in Figure 2. Recalling that $l_{PZ} = a_{max} - a_{min}$ directly leads to the

conclusion, that the range of \hat{a} must increase as the length of the process zone l_{PZ} increases, and the range of observed difference in the resulting $G_{Ic,ASTM}$ increases accordingly. Any difference should dissipate as the crack grows since

$$\lim_{(\Delta a/\hat{a}) \rightarrow \infty} \frac{a_0 + \Delta a}{a_0 + \Delta a + \hat{a}} = 1 \quad (16)$$

However, since fiber bridging, in combination with a honeycomb core, leads to relatively high CERR at relatively low homogenized strength, the process zone length, l_{PZ} , can be relatively long, even when common cohesive laws are considered. This can invalidate Eq. (16), for instance, if l_{PZ} , and thus the possible range of \hat{a} , is of the same order of magnitude as the specimen length. The investigation of consistent, feasible crack criteria is even more important, when an unconventional cohesive law is to be validated. Therefore, a consistent and direct definition of the crack length, in a numerical context, becomes necessary in order to compare the experimental results. In the CZM literature, the crack tip position is most commonly considered to correspond to the first point in the wake of the crack that exhibits damage [16]. However, usually this crack length is not used for numerical apparent CERR calculations. In the present study, this criterion yielded results that qualitatively differed from experiments and that were highly sensitive with respect to the cohesive strength.

Indirect compliance-based methods as proposed in [32, 67] are not feasible for crack length determination in this context. For these methods, an assumption about the cohesive law shape [67], or even about the R-curve directly [32], has to be made. Determining which shape is most appropriate for the considered application is the subject of the present investigation. Assuming the shape upfront would therefore lead to a circular argument.

The five aforementioned options were studied, and the most consistent results were achieved with option 3, i.e. a dissipated energy threshold criterion. For convenience, the parameters θ_{Ic} and $\theta_{Ic,m}$,

$$\theta_{Ic} = \frac{G_{I,crack\ tip}}{G_{Ic}} \quad \theta_{Ic,m} = \frac{G_{I,crack\ tip}}{G_{Ic,m}} \quad (17)$$

which indicate the fraction of the CERR at which the crack tip position is assumed, are introduced. A certain dissipated energy level, θ , is chosen, and the corresponding opening, δ_θ , is calculated as

$$\theta_{Ic} G_{Ic} = \int_0^{\delta_\theta} T_b(\delta_n) d\delta_n \quad \theta_{Ic,m} G_{Ic,m} = \int_0^{\delta_\theta} T_b(\delta_n) d\delta_n \quad (18)$$

The longitudinal position at which the specific opening value δ_θ is met is extracted from the FE output, and the apparent CERR, according to Eq. (15), is calculated along with the associated load and displacement values. This criterion provided the most consistent results for a wide range of strength values and cohesive law shapes and is therefore considered a robust engineering estimate of the apparent energy release rate. While the measured value is an opening value, i.e. a relative displacement of the upper lever and the core, it is not an opening threshold criterion in the

sense of item 1 of the previously given list, since the δ_θ value is not a constant, but is unique for every cohesive law.

Figure 17 shows a comparison of the experimentally obtained R-curves and the numerical counterparts extracted according to the described method for $\theta_{Ic,m} = 0.5$ of $G_{Ic,m}$, $\theta_{Ic,m} = 0.55$, and $\theta_{Ic,m} = 0.667$, respectively. For reference, $\theta_{Ic,m} = 0.5$ corresponds to 50% of $G_{Ic,m}$, i.e. $0.5 \cdot 200 \text{ J/m}^2 / 1030 \text{ J/m}^2 = 9.71\%$ of G_{Ic} . All numerical and experimental curves are in good qualitative agreement. The initial increase, angular peak and slight post-peak decrease are all well-captured. The best quantitative agreement is achieved between a) the $\theta_{Ic,m} = 0.55$ criterion and the DIC 1% max. principal strain curves and b) the $\theta_{Ic,m} = 0.667$ criterion and the DIC 4% max. principal strain curves. The travelling telescope G_{Ic} values are approximately 3 – 5% lower in the post-peak region. This is likely due to oblique crack growth. However, the qualitative agreement is still good. It is of note that the apparent fracture toughness is more than 10% higher than the constitutive fracture toughness at 45 mm crack length. The G_{Ic} -peak occurs when the bridging zone is fully formed shortly before the fully developed zone begins to propagate self-similarly, see Figures 15 d)-e). Figures 18-20 provide the same R-curve comparisons to the test data as

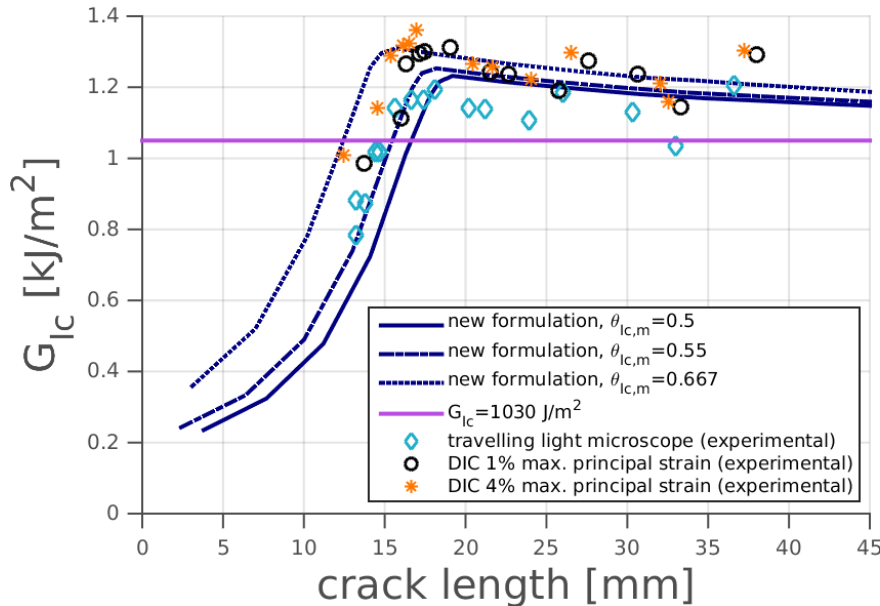


Figure 17: Comparison of experimental and numerical R-curves obtained with the new cohesive formulation.

Figure 17, but now for the existing cohesive formulations examined in Section 6.1. Qualitatively, these figures are mutually similar but clearly distinct from Figure 17. The angular shaped pre-peak/post-peak transition can generally not be captured. Only the bilinear formulation (Fig. 18) has an angular shaped transition in the case of $T^{max} = 2.0 \text{ MPa}$. However, due to the relatively high strength, the peak is at approximately half the crack length that was observed in the experiment. The parameters that matched the peak load (bold blue lines) underestimate the apparent

CERR obtained through the DIC measurements for all criteria and formulations. The travelling telescope values are underestimated when the $\theta_{Ic} = 0.1$ crack length criterion is used. When the $\theta_{Ic} = 0.2$ crack length criterion is employed, the peak values are matched better, but the pre-peak values are severely overestimated. The bilinear and exponential formulations also show some deviation from the constitutive CERR (1050 J/m^2) over the entire considered crack length, although not as pronounced as in the case of the newly proposed formulation. No substantial discrepancy between constitutive and apparent CERR is observed in the case of the PPR formulation beyond 30 mm crack length. This indicates that the experimental apparent CERR values are underpredicted, as the apparent experimental CERR are generally higher than the constitutive CERR, once the crack is fully developed. The experimental R-curve shape and the R-curve shapes of the new formulation do not directly correspond to one of the three cases of R-curves identified by Spearing and Evans [66]. Out of the three identified cases, the current results appear most like the “perfectly plastic” cases, except that the R-curve is more peaked in the regime of the greatest load. It is of note, that if a maximum initial stress (equivalent damage onset) criterion is used, all formulations fall between the “strain softening” and “linear elastic” case outlined in [66]. The R-curve bears some resemblance to the long pre-cut notch case identified by Jacobsen and Sørensen [68], including the “overshoot”.

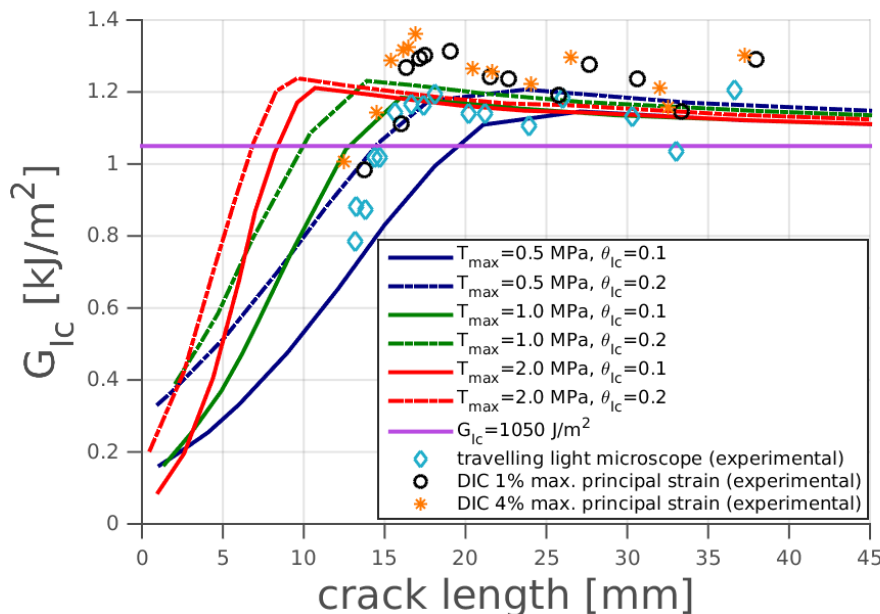


Figure 18: Comparison of experimental and numerical R-curves obtained with the bilinear COH2D4 formulation.

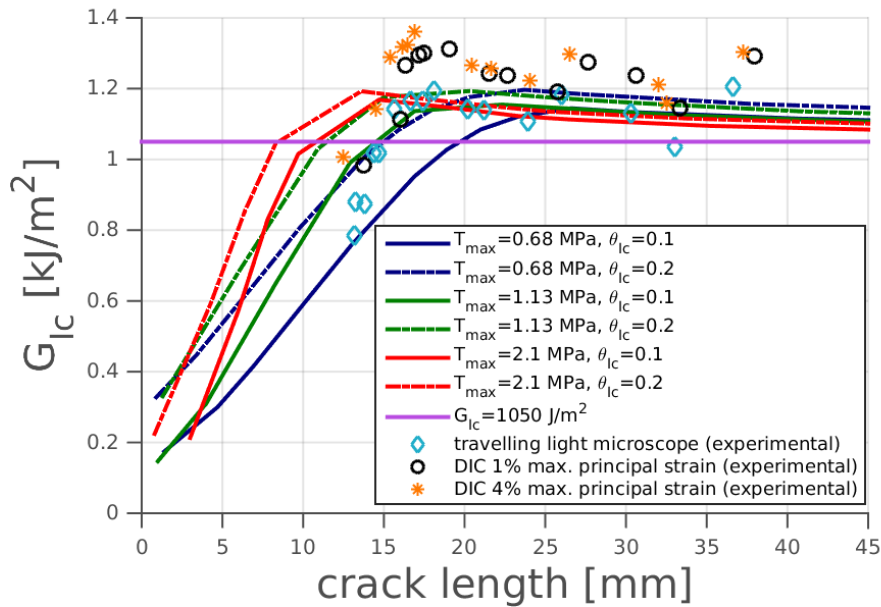


Figure 19: Comparison of experimental and numerical R-curves obtained with the exponential COH2D4 formulation.

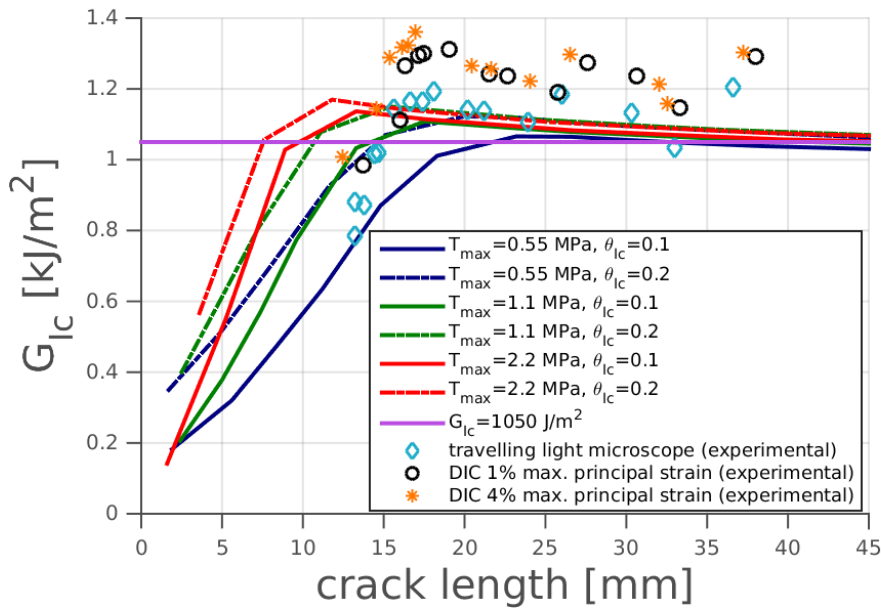


Figure 20: Comparison of experimental and numerical R-curves obtained with the PPR cohesive formulation.

Figures 17-20 emphasize that the apparent CERR is significantly different from the constitutive CERR for all considered formulations. Furthermore, the short pro-

cess zone argument implicit in Eq. (16) can clearly not be made for the results herein. The difference is most pronounced for the newly developed formulation. This new formulation has the clear advantage that it provides two separate components for matrix cracking/fiber disbond-related damage on the one hand, and fiber bridging-related damage on the other hand. Employing a 10% and 20% of the total CERR criterion only on the bridging component of the cohesive law was found to be insufficient. Therefore, it was shown that both the matrix and bridging parts are necessary for an accurate prediction of a consistent crack length. The proposed procedure is shown to provide useful engineering estimates for the apparent fracture toughnesses values of the FE calculations in the current example. An interesting point for future research is how good the agreement between the proposed engineering estimates and more elaborate implicit methods, as proposed by Leone et al. [38] and Sarrado et al. [39], is.

7 Conclusion

A novel cohesive formulation for delamination modeling, in which the interfacial cracking and fiber bridging mechanisms are considered separately, has been proposed and applied to facesheet-core debonding in aluminum honeycomb sandwich panels. The proposed formulation consists of an initial matrix component as well as a bridging component, which develops traction as the separation increases, representing the traction transferred by bridging fibers after the rotation process. The results obtained with the proposed formulation are in very good agreement with experimental load-displacement curves obtained from SCB tests. Furthermore, the newly proposed formulation captures the concave downward / concave upward pre-peak shape of the load-displacement curve that is observed while the fiber bridging is developing. Existing standard cohesive formulations are unable to capture this phenomenon. Specimens exhibiting long process zones do not have a clear crack tip with a traction-free surface in its wake due to the presence of substantial fiber bridging. The experimental strain distribution in the wake of the crack front exhibited two distinct zones of high strain. The two zones were captured by the newly developed cohesive zone formulation, but not by the existing cohesive zone formations. A simple engineering approach for the estimation of the R-curve based on FE data was presented and validated. Finally, it was shown that the new method has excellent numerical performance.

Appendix A

Additional analytical expressions related to T_b

Finding analytical expressions for the characteristic quantities listed in Table 1 can be quite impractical for T_b . This is caused by term (b) in Eq. (4), which even for integer exponents q and r leads to a variable number of terms as prescribed by Pascal's triangle. Since δ_b^f is a rather useful quantity for implementation purposes it is given here for the specific exponents $q = 3$ and $r = 1$, which are considered throughout this paper.

$$\begin{aligned} \delta_b^f = & \delta_b^p/3 + (((3 * \delta_b^{0^2} * \delta_b^p)/2 + (\delta_b^0 * \delta_b^{p^2})/2 + \delta_b^{p^3}/27)^2 - (\delta_b^{p^2}/9 + \delta_b^0 * \delta_b^p)^3)^{(1/2)} + \\ & (\delta_b^0 * \delta_b^{p^2})/2 + (3 * \delta_b^{0^2} * \delta_b^p)/2 + \delta_b^{p^3}/27)^{(1/3)} + (\delta_b^{p^2}/9 + \delta_b^0 * \delta_b^p)/(((3 * \delta_b^{0^2} * \delta_b^p)/2 + \\ & (\delta_b^0 * \delta_b^{p^2})/2 + \delta_b^{p^3}/27)^2 - (\delta_b^{p^2}/9 + \delta_b^0 * \delta_b^p)^3)^{(1/2)} + (\delta_b^0 * \delta_b^{p^2})/2 + (3 * \delta_b^{0^2} * \delta_b^p)/2 + \\ & \delta_b^{p^3}/27)^{(1/3)} \end{aligned} \tag{A1}$$

Both Matlab and Mathematica performed well in providing analytical expressions for all relevant characteristic quantities. However, the authors were not able to simplify the results to a form which provides further insight into the problem and the other characteristic quantities (highest traction value, fracture toughness) are therefore not reported, but can easily be obtained for specific exponent choices with said programs.

Appendix B

Further cohesive parameters

Table B1: Cohesive parameters used in Figure 8.

	T^{max} [MPa]	G_{Ic} [KJ/m ²]	stiffness in the origin K_0 [MPa/mm]
COH2D4 bilinear #1	2.0	1045	75
COH2D4 bilinear #2	1.5	1045	70
COH2D4 bilinear #3	1.05	1045	40
COH2D4 bilinear #4	0.75	1045	75
COH2D4 bilinear #5	0.6	1045	75
COH2D4 bilinear #6	0.5	1045	75
COH2D4 bilinear #7	0.3	1045	75

Table B2: Best fit cohesive parameters for 3 established element formulations used in Figures 9(a)-9(b).

	common parameters			model-specific parameters	
	T^{max} [MPa]	G_{Ic} [KJ/m ²]	K_0 [MPa/mm]		
COH2D4 bilinear #6	0.5	1045	75		
COH2D4 exponential	0.675	(1047)	67.5	α [-] 5.0	
User element PPR	0.53	1050	(73.25)	α [-] 3.0	β [-] 3.0

Appendix C

Symbols

\mathbf{C}	elasticity tensor	[MPa]
C_b	cohesive parameter	[MPa]
\hat{C}_b	cohesive parameter of the alternative bridging component	[MPa]
E	Young's modulus	[MPa]
G	shear modulus	[MPa]
G_{Ic}	mode I critical energy release rate	[kJ/m ²]
$G_{Ic,ASTM}$	apparent mode I critical energy release rate determined according to ASTM D 5528	[kJ/m ²]
$G_{Ic,b}$	constitutive mode I critical energy release rate of the bridging cohesive component	[kJ/m ²]
$G_{Ic,const}$	constitutive mode I critical energy release rate	[kJ/m ²]
$G_{Ic,m}$	constitutive mode I critical energy release rate of the initial interface cohesive component	[kJ/m ²]
K_0	cohesive penalty stiffness	[MPa]
M	process zone length parameter	[-]
P	load	[N]
S	surface	[m ²]
T	total traction	[MPa]
T_b	bridging component of the cohesive traction	[MPa]
\hat{T}_b	alternative bridging component of the cohesive traction	[MPa]
T_c	cohesive traction	[MPa]
\mathbf{T}_{ext}	vector of external tractions	[MPa]
T_m	initial interface component of the cohesive traction	[MPa]
T_m^{max}	initial interface component strength	[MPa]
T_n	normal cohesive traction component	[MPa]
T_s	tangential cohesive traction component	[MPa]
V	volume	[m ³]
a_0	insert (initial) crack length	[mm]
Δa	crack growth length	[mm]
\hat{a}	crack position uncertainty	[mm]
a_{min}	smallest conceivable crack length	[mm]
a_{max}	greatest conceivable crack length	[mm]
\mathbf{f}_{coh}	cohesive traction vector	[MPa]
l_{PZ}	process zone length	[mm]
u	loading point displacement	[mm]
\mathbf{u}	displacement vector	[mm]
q	cohesive law exponent parameter	[-]

\hat{q}	cohesive law exponent parameter of the alternative bridging component	[-]
r	cohesive law exponent parameter	[-]
\hat{r}	cohesive law exponent parameter of the alternative bridging component	[-]
Γ	domain boundary	[m ²]
Γ_c	potential fracture surface	[m ²]
Ω	domain	[m ³]
α	cohesive parameter	[-]
β	cohesive parameter	[-]
δ_b^0	cohesive parameter	[mm]
δ_b^p	cohesive parameter	[mm]
δ_b^f	failure strain	[mm]
$\hat{\delta}_b^f$	failure strain of the alternative bridging component	[mm]
δ_m^0	cohesive parameter	[mm]
δ_n	normal separation	[mm]
δ_s	tangential separation	[mm]
δ_θ	crack identification opening	[mm]
ε	strain tensor	[-]
ν	Poisson ratio	[-]
σ	stress tensor	[MPa]
θ_{Ic}	G_{Ic} -based crack identification parameter	[-]
$\theta_{Ic,m}$	$G_{Ic,m}$ -based crack identification parameter	[-]

References

1. Raju, K. S.; Smith, B. L.; Tomblin, J. S.; Liew, K. S.; and Guarddon, J. C.: Impact Damage Resistance and Tolerance of Honeycomb Core Sandwich Panels. *Journal of Composite Materials*, vol. 42, 2008, pp. 385–412.
2. McQuigg, T. S.; Kapania, R. K.; Scotti, S. J.; and Walker, S. P.: Compression After Impact on Honeycomb Core Sandwich Panels with Thin Facesheets, Part 1: Experiments. *53rd AIAA/ASME/ASCE/AHS/ASC Structures, Structural Dynamics, and Materials Conference*, 2012.
3. Ratcliffe, J. G.; and Jackson, W. C.: A Finite Element Analysis for Predicting the Residual Compressive Strength of Impact-Damaged Sandwich Panels. *NASA/TM-2008-215341*, 2008.
4. Lacy, T. E.; and Hwang, Y.: Numerical Modeling of Impact-Damaged Sandwich Composites Subjected to Compression-After-Impact Loading. *Composite Structures*, vol. 61, 2003, pp. 115–128.
5. Hodge, A.; Nettles, A.; and Jackson, J.: Comparison of Open-Hole Compression Strength and Compression After Impact Strength on Carbon Fiber/Epoxy Laminates for the Ares I Composite Interstage. *NASA/TP-2011-216460*, 2001.
6. McQuigg, T.: Compression After Impact Experiments and Analysis on Honeycomb Core Sandwich Panels with Thin Facesheets. *NASA/CR-2011-217157*, 2011.
7. Zalewski, B.; and Bednarczyk, B.: ACT Payload Shroud Structural Concept Analysis and Optimization. *NASA/TM-2010-216942*, 2010.
8. Pineda, E.; Myers, D.; Kosareo, D.; Zalewski, B.; and Dixon, G.: Buckling Testing and Analysis of Honeycomb Sandwich Panel Arc Segments of a Full-Scale Fairing Barrel Part 2: 6-Ply In-Autoclave Facesheets. *NASA/TM-2013-217822/PART2*, 2013.
9. Pineda, E.; Myers, D.; Kasareo, D.; and Kellas, S.: Buckling Testing and Analysis of Honeycomb Sandwich Panel Arc Segments of a Full-Scale Fairing Barrel Part 3: 8-Ply Out-of-Autoclave Facesheets. *NASA/TM-2014-217822/PART3*, 2014.
10. Pineda, E.; Bednarczyk, B.; and Krivanek, T.: Post-Buckling Analysis of Curved Honeycomb Sandwich Panels Containing Intefacial Disbonds. *Proc. AIAA SciTech Conference, San Diego, CA, 4-8 Jan.*, 2016.
11. Camanho, P. P.; Dávila, C. G.; and de Moura, M. F.: Numerical Simulation of Mixed-Mode Progressive Delamination in Composite Materials. *Journal of Composite Materials*, vol. 37, 2003, pp. 1415–1438.
12. Turon, A.; Camanho, P.; Costa, J.; and Dávila, C.: A damage model for the simulation of delamination in advanced composites under variable-mode loading. *Mechanics of Materials*, vol. 38, 2006, pp. 1072–1089.

13. Li, S.; Thouless, M.; Waas, A.; Schroeder, J.; and Zavattieri, P.: Use of mode-I cohesive-zone models to describe the fracture of an adhesively-bonded polymer-matrix composite. *Composites Science and Technology*, vol. 65, 2005, pp. 281–293.
14. Li, S.; Thouless, M.; Waas, A.; Schroeder, J.; and Zavattieri, P.: Use of a cohesive-zone model to analyze the fracture of a fiber-reinforced polymer-matrix composite. *Composites Science and Technology*, vol. 65, 2005, pp. 537–549.
15. Li, S.; Thouless, M.; Waas, A.; Schroeder, J.; and Zavattieri, P.: Mixed-mode cohesive-zone models for fracture of an adhesively bonded polymer-matrix composite. *Engineering Fracture Mechanics*, vol. 73, 2006, pp. 64–78.
16. Dávila, C. G.; Rose, C. A.; and Camanho, P.: A procedure for superposing linear cohesive laws to represent multiple damage mechanisms in the fracture of composites. *International Journal of Fracture*, vol. 158, 2009, pp. 211–223.
17. Airoidi, A.; and Dávila, C. G.: Identification of material parameters for modelling delamination in the presence of fibre bridging. *Composite Structures*, vol. 94, no. 11, 2012, pp. 3240–3249.
18. Gutkin, R.; Laffan, M.; Pinho, S.; Robinson, P.; and Curtis, P.: Modelling the R-curve effect and its specimen-dependence. *International Journal of Solids and Structures*, vol. 48, 2011, pp. 1767–1777.
19. El-Sayed, S.; and Sridharan, S.: Predicting and tracking interlaminar crack growth in composites using a cohesive layer model. *Composites Part B: Engineering*, vol. 32, no. 6, 2001, pp. 545–553.
20. Sørensen, B. F.; and Jacobsen, T. K.: Large-scale bridging in composites: R-curves and bridging laws. *Composites Part A*, vol. 29A, 1998, pp. 1443–1451.
21. Lu, X.; Teng, J.; Ye, L.; and Jiang, J.: Bond-slip models for sheets/plates bonded to concrete. *Engineering Structures*, vol. 27, 2005, pp. 938–950.
22. Neale, K. W.; Ebead, U. A.; Baky, H. M. A.; Elsayed, W. E.; and Godat, A.: Analysis of the Load-Deformation Behaviour and Debonding for FRP-Strengthened Concrete Structures. *Advances in Structural Engineering*, vol. 9, 2006, pp. 751–763.
23. Feih, S.: Development of a user element in ABAQUS for modelling of cohesive laws in composite structures. *Risø-R Report*, vol. 1501(EN), 2005, pp. 1–52.
24. Park, K.; and Paulino, G. H.: Computational implementation of the PPR potential-based cohesive model in ABAQUS: Educational perspective. *Engineering Fracture Mechanics*, vol. 93, 2012, pp. 239–262.
25. Turon, A.; Dávila, C.; Camanho, P.; and Costa, J.: An engineering solution for mesh size effects in the simulation of delamination using cohesive zone models. *Engineering Fracture Mechanics*, vol. 74, 2007, pp. 1668–1682.

26. Remmers, J. J. C.; Wells, G. N.; and de Borst, R.: A solid-like shell element allowing for arbitrary delaminations. *International Journal for Numerical Methods in Engineering*, vol. 58, 2003, pp. 2013–2040.
27. Mohammadi, B.; and Salimi-Majd, D.: Investigation of delamination and damage due to free edge effects in composite laminates using cohesive interface elements. *Engineering Solid Mechanics*, vol. 2, 2014, pp. 101–118.
28. Guiamatsia, I.; and Nguyen, G. D.: A generic approach to constitutive modelling of composite delamination under mixed-mode loading conditions. *Composites Science and Technology*, vol. 72, 2012, pp. 269–277.
29. Simon, J.-W.; Höwer, D.; Stier, B.; Reese, S.; and Fish, J.: A regularized orthotropic continuum damage model for layered composites: intralaminar damage progression and delamination. *Computational Mechanics*, 2017, pp. 1–17.
30. Simon, J.-W.; Höwer, D.; Stier, B.; and Reese, S.: Meso-mechanically motivated modeling of layered fiber reinforced composites accounting for delamination. *Composite Structures*, vol. 122, 2015, pp. 477–487.
31. Reinoso, J.; Paggi, M.; and Blázquez, A.: A nonlinear finite thickness cohesive interface element for modeling delamination in fibre-reinforced composite laminates. *Composites Part B: Engineering*, vol. 109, 2016, pp. 116–128.
32. Heidari-Rarani, M.; Shokrieh, M.; and Camanho, P.: Finite element modeling of mode I delamination growth in laminated DCB specimens with R-curve effects. *Composites Part B: Engineering*, vol. 45, no. 1, feb 2013, pp. 897–903.
33. Xie, D.; Salvi, A. G.; Sun, C.; Waas, A. M.; and Caliskan, A.: Discrete Cohesive Zone Model to Simulate Static Fracture in 2D Triaxially Braided Carbon Fiber Composites. *Journal of Composite Materials*, vol. 40, 2006, pp. 2025–2046.
34. Wong, K. J.; Gong, X. J.; Aivazzadeh, S.; and Tamin, M. N.: Numerical simulation of mode I delamination behaviour of multidirectional composite laminates with fibre bridging effect. *ECCM - 15th European conference on composite materials, Venice, Italy, 24-28 June 2012*, 2012.
35. Rice, J.: A path independent integral and the approximate analysis of strain concentration by notches and cracks. *Journal of Applied Mechanics*, vol. 35, 1968, pp. 379–386.
36. Jacobsen, T.; and Sørensen, B.: Mode I intra-laminar crack growth in composites - modelling of R-curves from measured bridging laws. *Composites Part A: Applied Science and Manufacturing*, vol. 32, 2001, pp. 1–11.
37. Leone, F. A.; Girolamo, D.; and Dávila, C. G.: Progressive Damage Analysis of Bonded Composite Joints. *NASA/TM-2012-217790*, 2012, pp. 1–39.
38. Leone, F. A.; Dávila, C. G.; and Girolamo, D.: Progressive damage analysis as a design tool for composite bonded joints. *Composites Part B: Engineering*, vol. 77, 2015, pp. 474–483.

39. Sarrado, C.; Turon, A.; Renart, J.; and Costa, J.: An experimental data reduction method for the Mixed Mode Bending test based on the J-integral approach. *Composites Science and Technology*, vol. 117, 2015, pp. 85–91.
40. Cantwell, W.; Scudamore, R.; Ratcliffe, J.; and Davies, P.: Interfacial fracture in sandwich laminates. *Composites Science and Technology*, vol. 59, 1999, pp. 2079–2085.
41. Shanmugam, V.; Penmetsa, R.; Tuegel, E.; and Clay, S.: Stochastic modeling of delamination growth in unidirectional composite DCB specimens using cohesive zone models. *Composite Structures*, vol. 102, aug 2013, pp. 38–60.
42. Hsueh, C.-H.: Interfacial Debonding and Fiber Pull-out Stresses of Fiber-reinforced Composites. *Materials Science and Engineering*, vol. 123, 1990, pp. 1–11.
43. Tan, K.; Watanabe, N.; and Iwahori, Y.: Experimental investigation of bridging law for single stitch fibre using Interlaminar tension test. *Composite Structures*, vol. 92, 2010, pp. 1399–1409.
44. Höwer, D.; Stier, B.; Felder, S.; Simon, J.-W.; and Reese, S.: Mode I and II delamination modelling and comparison to experiments. *3rd ECCOMAS Young Investigators Conference July 20-23, 2015, Aachen, Germany*, 2015.
45. Canal, L.; Pappas, G.; and Botsis, J.: Large scale fiber bridging in mode I intralaminar fracture. An embedded cell approach. *Composites Science and Technology*, vol. 126, 2016, pp. 52–59.
46. Goutianos, S.; and Sørensen, B. F.: The application of J integral to measure cohesive laws under large-scale yielding. *Engineering Fracture Mechanics*, vol. 155, 2016, pp. 145–165.
47. Robinson, P.; and Das, S.: Mode I DCB testing of composite laminates reinforced with z-direction pins: a simple model for the investigation of data reduction strategies. *Engineering Fracture Mechanics*, vol. 71, 2004, pp. 345–364.
48. Carlsson, L. A.; Adams, D. F.; and Pipes, R. B.: *Experimental characterization of advanced composite materials*. CRC Press, 4th edition ed., 2014.
49. Sørensen, L.; Botsis, J.; Gmür, T.; and Humbert, L.: Bridging tractions in mode I delamination: Measurements and simulations. *Composites Science and Technology*, vol. 68, 2008, pp. 2350–2358.
50. Krull, B.; Patrick, J.; Hart, K.; White, S.; and Sottos, N.: Automatic Optical Crack Tracking for Double Cantilever Beam Specimens. *Experimental Techniques*, 2015, pp. 1–9.
51. Shokrieh, M.; Heidari-Rarani, M.; and Rahimi, S.: Influence of curved delamination front on toughness of multidirectional DCB specimens. *Composite Structures*, vol. 94, 2012, pp. 1359–1365.

52. Gong, X.; Hurez, A.; and Verchery, G.: On the determination of delamination toughness by using multidirectional DCB specimens. *Polymer Testing*, vol. 29, 2010, pp. 658–666.
53. Ratcliffe, J. G.; and Reeder, J. R.: Sizing a single cantilever beam specimen for characterizing facesheet-core debonding in sandwich structure. *Journal of Composite Materials*, vol. 45, 2011, pp. 2669–2684.
54. Rinker, M.; Ratcliffe, J. G.; Adams, D. O.; and Krueger, R.: Characterizing Facesheet/Core Disbonding in Honeycomb Core Sandwich Structure. *NASA/CR-2013-217959*, vol. NIA Report No. 2013-0115, 2013, pp. 1–35.
55. ASTM D 5528: Standard Test Method for Mode I Interlaminar Fracture Toughness of Unidirectional Fiber-Reinforced Polymer Matrix Composites. ASTM International, 2007.
56. Guinea, G.; Planas, J.; and Elices, M.: A general bilinear fit for the softening curve of concrete. *Materials and Structures*, vol. 27, 1994, pp. 99–105.
57. Turon, A.; Camanho, P.; Costa, J.; and Renart, J.: Accurate simulation of delamination growth under mixed-mode loading using cohesive elements: Definition of interlaminar strengths and elastic stiffness. *Composite Structures*, vol. 92, 2010, pp. 1857–1864.
58. Hillerborg, A.; Modéer, M.; and Petersson, P.-E.: Analysis of crack formation and crack growth in concrete by means of fracture mechanics and finite elements. *Cement and Concrete Research*, vol. 6, 1976, pp. 773–781.
59. Davidson, P.; Waas, A. M.; and Yerramalli, C. S.: Experimental determination of validated, critical interfacial modes I and II energy release rates in a composite sandwich panel. *Composite Structures*, vol. 94, 2012, pp. 477–483.
60. Park, K.; and Paulino, G. H.: Cohesive Zone Models: A Critical Review of Traction-Separation Relationships Across Fracture Surfaces. *Applied Mechanics Reviews*, vol. 64, 2012, pp. 1–20.
61. Sørensen, B. F.; and Jacobsen, T. K.: Determination of cohesive laws by the J integral approach. *Engineering Fracture Mechanics*, vol. 70, 2003, pp. 1841 – 1858.
62. Reeder, J. R.; and Rews, J. H.: Mixed-mode bending method for delamination testing. *AIAA Journal*, vol. 28, 1990, pp. 1270–1276.
63. Nguyen, N.; and Waas, A. M.: A novel mixed-mode cohesive formulation for crack growth analysis. *Composite Structures*, vol. 156, 2015, pp. 253–262.
64. Shivakumar, K.; and Smith, S. A.: An Evaluation of Data Reduction Methods for Opening Mode Fracture Toughness of Sandwich Panels. *Journal of Sandwich Structures & Materials*, vol. 38, 2005, pp. 655–668.

65. Suo, Z.; Bao, G.; and Fan, B.: Delamination R-curve phenomena due to damage. *Journal of the Mechanics and Physics of Solids*, vol. 40, 1992, pp. 1–16.
66. Spearing, S.; and Evans, A.: The role of fiber bridging in the delamination resistance of fiber-reinforced composites. *Acta Metallurgica et Materialia*, vol. 40, 1992, pp. 2191–2199.
67. Dias, G.; de Moura, M.; Chousala, J.; and Xavierb, J.: Cohesive laws of composite bonded joints under mode I loading. *Composite Structures*, vol. 106, 2013, pp. 646–652.
68. Jacobsen, T.; and Sørensen, B.: Mode I intra-laminar crack growth in composites - modelling of R-curves from measured bridging laws. *Composites: Part A*, vol. 32, 2001, pp. 1–11.

